JM PAPERS

Mixing enhancement of a compressible jet over a convex wall

Qing Wang[1], Feng Qu[1,†], Tianyu Wang[1], Di Sun[1] and Junqiang Bai[1]

[1]School of Aeronautics, Northwestern Polytechnical University, Xi'an 710072, PR China

A highly compressive effect would suppress the mixing of the shear layer in a convex wall jet. The spanwise distributed protrusions at the nozzle lip are employed to achieve mixing enhancement in this study. The mixing characteristics and enhancement mechanisms are numerically investigated by the delayed detached-eddy simulation method based on the two-equation shear-stress transport model. A widely applicable flow spatiotemporal analysis method, called proper orthogonal decomposition (POD), is used to gain further insight into the dynamical behaviours of the flow instability mode. The results reveal that the centrifugal effect maintains and amplifies the initial perturbations induced by the spanwise distributed heterogeneities, resulting in forced streamwise vortices. The instabilities induced by the streamwise vortices significantly increase the growth rate of the jet half-width and the shear layer vorticity thickness. The spanwise wavelength of the streamwise vortices is consistent with the spanwise distributed forced excitation. In addition, the spanwise meandering motion of the streamwise vortices is observed, which is usually associated with the streamwise travelling wave. This is further confirmed by the POD analysis of the spanwise velocity fluctuation in both stream-radial and stream-span sections. Also, the spatial distributions of the POD modes with the highest energy provide information on the secondary instability modes. Both sinuous and varicose types of disturbances are observed in the unforced jet, whereas the forced jet seems to be dominated by the sinuous type instability, which is more easily excited than the varicose type instability. Moreover, the turbulence intensity in the forced jet is also significantly enhanced as expected due to the earlier and stronger streamwise vortices and associated instabilities. The enhanced turbulent characteristics of the highly compressible condition tend to be isotropic, whereas in the unforced jet, it is anisotropic due to the strong compressibility suppressing the spanwise turbulent fluctuations.

Key words: high-speed flow

† Email address for correspondence: qufeng@nwpu.edu.cn

1. Introduction

The concept of fluidic control effectors, which could achieve the same function as conventional control surfaces, has an attractive prospect because it can significantly improve the aerodynamic, economic, comfortable and stealth performance of an aircraft (Warsop & Crowther 2018). The fluid control effectors usually employ the circulation control (CC) (Wilde *et al.* 2008; Crowther *et al.* 2009; Smith & Warsop 2019; Warsop, Crowther & Forster 2019) technology to achieve the lifting augmentation (Englar *et al.* 1981; Zhang *et al.* 2018), rolling and yawing control (Harley, Wilde & Crowther 2009; Hoholis, Steijl & Badcock 2016) (replacement of flaps, ailerons and rudders) and the fluidic thrust vector (FTV) (Ferlauto & Marsilio 2017; Li *et al.* 2017; Warsop & Crowther 2018) technology to achieve the pitching control (replacement of elevators) of the aircraft. The feasibility of these technologies has been verified in the ICE and SACCON unmanned aerial vehicles of the NATO task group AVT-239 (Hutchin 2019; Warsop *et al.* 2019; Williams *et al.* 2019). However, there are still many challenges to realize flapless flight control by adopting fluid control effectors on the full-scale aircraft. One of the difficulties is that the control efficiency is greatly reduced at transonic speeds. Under this condition, the problem of a supersonic jet over a convex wall is inevitable as both CC and FTV technologies are achieved through a Coanda effect. Therefore, it is necessary to thoroughly study the supersonic jet over a convex wall.

There are two important flow structures in the supersonic jet over a convex wall: the shock-wave/boundary-layer interaction (SWBLI) and shear layer in the outer region of the jet. The SWBLI makes the jet separate from the Coanda surface at a certain high jet pressure ratio, which leads to the failure of the CC and FTV technologies. To cure this deflect, many scholars have directed their attention on the SWBLI induced separation, and tried to improve the effective pressure ratio by carefully designing the geometry of the Coanda device. For example, Cornelius & Lucius (2012) adopted a converging–diverging nozzle to expand the jet and increase the pressure ratio at which the jet still remains attached compared with a converging only nozzle. Gregory-Smith & Senior (1994) and Carpenter & Green (1997) achieved the same effect as Cornelius & Lucius (2012) by setting a step between the nozzle exit and the Coanda surface. Forster & Steijl (2017) further verified the effectiveness of these methods in the supersonic Coanda jet under transonic free streams. Bevilaqua & Lee (1980) reported a characteristics design method that skews the velocity and pressure profile along the jet exit, resulting in a favourable velocity and pressure gradient at the Coanda surface to promote the jet attachment. Alexander *et al.* (2005) conducted parametric evaluations of the slot heights and the Coanda surface shapes in the NASA Langley Transonic Dynamics Tunnel. Forster, Biava & Steijl (2016) carried out multipoint optimization of the transonic CC airfoil Coanda surface. These explorations have improved the effective working pressure ratio, but the separation seems to be unavoidable. Therefore, it is an urgent need to further improve the control efficiency under the limited jet inlet pressure ratio.

In addition to the influence of the wave structures, the shear layer plays an important role in the supersonic Coanda jet as well. The entrainment of the shear layer dominates the momentum exchange between the jet and the outflow. Different from the well-studied planar mixing layer, there are not only the Kelvin–Helmholtz type inflectional instability (Neuendorf & Wygnanski 1999; Watanabe & Nagata 2021), but also the Taylor–Görtler type of centrifugal instability (Görtler 1941; Cunff & Zebib 1996; Matsson & John 1998) in the curved jet shear layer. A series of previous studies have shown that this additional centrifugal instability plays an important role in the development of a convex wall jet (Fujisawa & Kobayashi 1987; Neuendorf & Wygnanski 1999; Likhachev, Neuendorf &

Wygnanski 2001; Neuendorf, Lourenco & Wygnanski 2004; Han, De Zhou & Wygnanski 2006; Dunaevich & Greenblatt 2020; Pandey & Gregory 2020, 2021). Fujisawa & Kobayashi (1987), Neuendorf & Wygnanski (1999) and Likhachev *et al.* (2001) found that the jet spreading rate and turbulence intensity of the curved jet were significantly enhanced in comparison with the corresponding plane jet. The streamwise vortices induced by the centrifugal effect are considered to be responsible for the mixing enhancement in the curved jet. Dunaevich & Greenblatt (2020) firstly observed the spontaneously generated stationary streamwise structures using flow visualization and particle image velocimetry. These structures ultimately exhibited a secondary time-dependent wavy instability. Pandey & Gregory (2020) confirmed the existence of the wavy instability in a forced jet over a convex wall by proper orthogonal decomposition (POD) analysis of the spanwise velocity fluctuation. Also, the conditional averaging analysis showed that the wavy instability was dominated by the sinuous type instability. However, all these findings were obtained in the incompressible convex wall jet. In the compressible curved shear flow, Gregory-Smith & Gilchrist (1987) and Gregory-Smith & Senior (1994) experimentally studied a supersonic jet over a convex wall and found that the outer shear layer grew more quickly than that of a plane jet. They also observed longitudinal streaks on the conical surface using surface oil flow visualization, which suggested the existence of the longitudinal Görtler-like vortices. Sun, Sandham & Hu (2019) and Wang *et al.* (2019) used direct numerical simulation (DNS) to study supersonic turbulent flows over concave surfaces. Large-scale streaks and turbulence amplification, Görtler-like vortices generated by the centrifugal effects were observed. These works reveal the important role of streamwise vortices caused by centrifugal instability in curved shear flow. Further, our previous work (Wang *et al.* 2023) on the compressible curved wall jet has shown that the highly compressibility effect would inhibit the generation of large-scale streamwise vortices as well as the growth of the shear layer. This suppressed shear layer would reduce the control efficiency of CC and FTV. However, Han *et al.* (2006) and Pandey & Gregory (2020, 2021) used spanwise heterogeneities at the nozzle lip of a cylinder apparatus to force streamwise vortices in a incompressible convex wall jet, and found that these vortices were subsequently sustained by the centrifugal effects. Also, Pandey & Gregory (2020) found that the turbulent fluctuations in a forced jet are stronger than that of an unforced jet. Inspired by the work of Han *et al.* (2006) and Pandey & Gregory (2020, 2021), this study explores the establishment of spanwise heterogeneities at the nozzle lip to induce the generation of the streamwise vortices and accelerate the instability of the compressible jet shear layer, so as to enhance the mixing capacity. The overall goal of this paper is to study the mixing characteristics and enhancement mechanism by adopting spanwise heterogeneities at the nozzle lip.

High-fidelity simulations of the turbulence in the boundary layer are extremely expensive using DNS or large eddy simulation (LES) with near wall resolution methods (Spalart *et al.* 2006). Recently, Naqvi, Tyacke & Tucker (2018) numerically studied a plane wall jet of $Re_j = U_j h/\nu = 7200$ (where h is the slot height, U_j is the jet slot exit velocity and ν is the kinematic viscosity). They employed $1652 \times 344 \times 302$ grid points in the streamwise, wall-normal and spanwise directions, respectively, which results in approximately 172×10^6 cells. However, for the supersonic jet in this study, $Re_j = U_j h/\nu = 218\,000$ (based on the slot height, and the sound speed of the ambient air), which is at least 30 times that of Naqvi *et al.* (2018). The huge number of grids caused by the high Reynolds number ($N \sim Re^{9/4}$, where N represents the number of grids) (Moin & Mahesh 1998) makes the expensive computational consumption unaffordable. Since we mainly focus on the behaviours of the shear layer in the compressible convex wall jet,

the detached eddy simulation (DES) method, which is a hybrid of the Reynolds-averaged Navier–Stokes (RANS) and LES, is an appropriate approach to avoid the massive resolution in the boundary layer. Therefore, the delayed detached-eddy simulation (DDES) method developed from the DES method, is adopted to study the supersonic jet over the convex wall in this paper. In addition, a widely applicable flow spatiotemporal analysis method, POD (Lumley 1967), is used to decompose the flow field and gain further insight into the dynamical behaviours.

This manuscript is organized as follows. Section 2 describes the details of numerical methods. In § 3, computational details are described. Numerical results and analysis are presented in § 4. The last section contains the main conclusions.

2. Numerical methods

All numerical simulations in this study are conducted by an in-house three-dimensional cell-centred finite volume solver developed by the authors. The solver has been successfully applied to considerable numerical studies on subsonic flows (Qu & Sun 2017), supersonic flows (Qu *et al.* 2019*b*; Sun *et al.* 2020), hypersonic flows (Sun, Qu & Yan 2018; Qu *et al.* 2019*a*) and supersonic Coanda flow (Wang *et al.* 2022, 2023). For simplicity, the main algorithms of the solver are represented as follows.

2.1. *Delayed detached-eddy simulation*

The basic governing equations are the RANS equations. For the additional Reynolds stress in the RANS equations, researchers have constructed many turbulence models to solve it. The shear-stress transport (SST) (Menter 1994) turbulence model is adopted in this paper.

The two-equation SST DDES method is implemented by modifying the dissipation-rate term of the turbulent kinetic energy transport equation as follows:

$$\frac{\partial(\rho k)}{\partial t} + \frac{\partial(\rho U_i k)}{\partial x_i} = \widetilde{P}_k - \frac{\rho k^{3/2}}{l_{hybrid}} + \frac{\partial}{\partial x_i}\left[(\mu + \sigma_k \mu_t)\frac{\partial k}{\partial x_i}\right], \tag{2.1}$$

$$\frac{\partial(\rho \omega)}{\partial t} + \frac{\partial(\rho U_i \omega)}{\partial x_i} = \frac{\gamma}{\nu_t}\widetilde{P}_k - \beta\rho\omega^2 + \frac{\partial}{\partial x_i}\left[(\mu + \sigma_\omega \mu_t)\frac{\partial \omega}{\partial x_i}\right] + 2(1-F_1)\rho\frac{\sigma_{\omega 2}}{\omega}\frac{\partial k}{\partial x_i}\frac{\partial \omega}{\partial x_i}, \tag{2.2}$$

where k and ω represent the turbulent kinetic energy and specific dissipation rate, respectively. The β is a constant, and the value of β is recommended as 0.09 by Menter (Fan *et al.* 2004). Here l_{hybrid} is the length scale defined as

$$l_{hybrid} = \min\{l_{RANS}, l_{LES}\}, \tag{2.3}$$

$$l_{RANS} = \frac{k^{1/2}}{\beta\omega}, \quad l_{LES} = C_{DES}\Delta = C_{DES}\max\{\Delta_x, \Delta_y, \Delta_z\}, \tag{2.4a,b}$$

in which l_{RANS} and l_{LES} are the length scales of the RANS turbulence model and LES method, respectively. Here Δ is the grid-scale, which is equal to the maximum grid spacing in x, y and z directions for the structured grid. Here C_{DES} is an empirical constant that needs to be calibrated and verified, reflecting the degree of dissipation in different computational fluid dynamics codes. As for the SST turbulence model, $C_{DES} = (1 - F_1)C_{DES}^{outer} + F_1 C_{DES}^{inner}$, where C_{DES}^{outer} is equal to 0.61, the C_{DES}^{inner} is equal to 0.78, and the F_1 is the internal function (Spalart *et al.* 2006) in the SST turbulence model.

However, the DES method suffers from modelled-stress depletion which will produce the grid induced separation. To overcome this problem, Spalart *et al.* (2006) proposed a new method named DDES by constructing a delayed function. The length scale of DDES can be expressed as follows:

$$
\left.
\begin{aligned}
l_{hybrid} &= l_{RANS} - f_d \max\{0, l_{RANS} - l_{LES}\}, \\
f_d &= 1 - \tanh\left[(8r_d)^3\right], \\
r_d &= \frac{\nu + \nu_t}{\sqrt{u_{i,j}u_{i,j}}\kappa^2 d^2},
\end{aligned}
\right\}
\tag{2.5}
$$

where the f_d is the delayed function, ν_t is the kinematic eddy viscosity, ν is the molecular viscosity, $u_{i,j}$ are the velocity gradients, κ is the Kármán constant of 0.41 and d is the distance to the wall. The structure of the delay function and the meaning of the parameters are detailed in Spalart *et al.* (2006). In case the f_d tends to 0, the RANS calculation is used. And in case the f_d tends to 1, the DDES method is converted to the traditional DES method.

2.2. *Numerical issues*

Spatial discretization resolution is critical for a high-fidelity numerical simulation. To level down the numerical dissipation, the inviscid fluxes are computed via the Roe flux-difference upwind scheme with the fifth-order weighted essential non-oscillatory (Liu, Osher & Chan 1994). The viscid fluxes are discretized by the fourth-order central differencing scheme. The fully implicit lower–upper symmetric Gauss–Seidel time-marching scheme (Yoon & Jameson 1988) with a second-order dual time-stepping method and Newton's subiteration for the inner loop is employed for time marching to achieve unsteady simulation.

In order to accelerate the formation of unsteady turbulent motions, all unsteady DDES simulations were initialized with corresponding converged steady RANS solutions. The unsteady DDES calculations are implemented with a fixed physical time-step size of 1.44×10^{-7} s. A maximum of 10 subiterations per time-step was used, resulting in a residual drop of at least 2–3 orders. After the transient flow with 25 000 steps, the remaining 10 000 steps are taken to obtain sufficient unsteady flow data per 25 steps for statistical analysis. The total physical time of 10 000 steps allows the fluid to flow over 2.5 times the arclength of the convex wall at the characteristic velocity (sound speed) to ensure that the periodic motions of the typical coherent structures can be effectively captured.

3. Computational details

3.1. *Model, flow conditions and boundary conditions*

The apparatus used in this study includes a convergent–divergent nozzle and a curved Coanda surface. The convergent–divergent nozzle is designed using a quasi-one-dimensional method based on isentropic flow theory without boundary layer corrections. The geometric tangency of the positions (i.e. the throat, the connection between the nozzle exit and Coanda surface), where the area changes, are ensured to eliminate the influence of geometric mutation on the flow. In addition, a symmetrical shape is used in upper and lower nozzle surfaces. The nozzle exit height is 10 mm, and the designed nozzle pressure ratio is 7 ($NPR_d = 7$). The Coanda surface is a $90°$
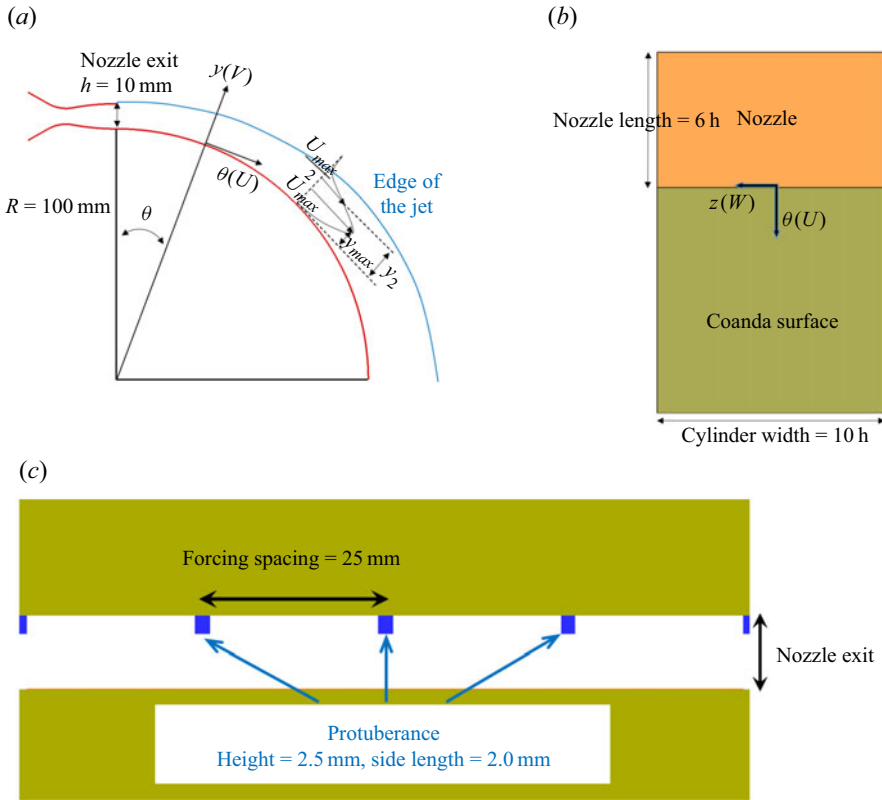
(*a*)

(*b*)

(*c*)

Figure 1. Schematics of the coordinate system and geometric characteristics: (*a*) side view; (*b*) top view, (*c*) protuberances at the nozzle lip.

circular arc with a radius of 100 mm fixing the h/R ratio to 0.1. Experiments were conducted by Llopis-Pascual (2017) at the University of Manchester. They obtained the pressure coefficient distribution of the Coanda surface and the Schlieren photograph of the jet. Unfortunately, there are not any measurements of the turbulence statistics and spanwise three-dimensional characteristics of the jet. As the experiments were carried out in quiescent air, the test conditions were $p_{amb} = 100$ kPa, $T_{amb} = 300$ K.

The geometric characteristics of the device and the cylindrical coordinate axes employed in this study are shown in figure 1. Azimuthal (θ), radial (y) and spanwise (z) coordinates correspond to the U, V and W components of velocity, respectively. The jet half-width (y_2), which is the wall-normal location where the streamwise velocity is half ($0.5U_{max}$) of its maximum value, is used as a measure of the jet thickness. Spanwise distributed cube protrusions are introduced in the upper nozzle lip to force initial disturbances (figure 1c). Refer to the size setting of the disturbance elements in the incompressible jet over a convex wall in Pandey & Gregory (2020). These disturbance elements are of side length 2 mm and protrude 2.5 mm (0.25 h) into the nozzle flow. The spanwise forcing wavelength is 25 mm.

The computational domain and boundary conditions are shown schematically in figure 2. Since the experiment device was fixed on a wall, the no-slip wall boundary conditions are applied at the side of the jet inlet. The pressure outlets ($p/p_{amb} = 1$) are employed for the other far boundary. Periodic boundary conditions are applied in the

972 A2-6
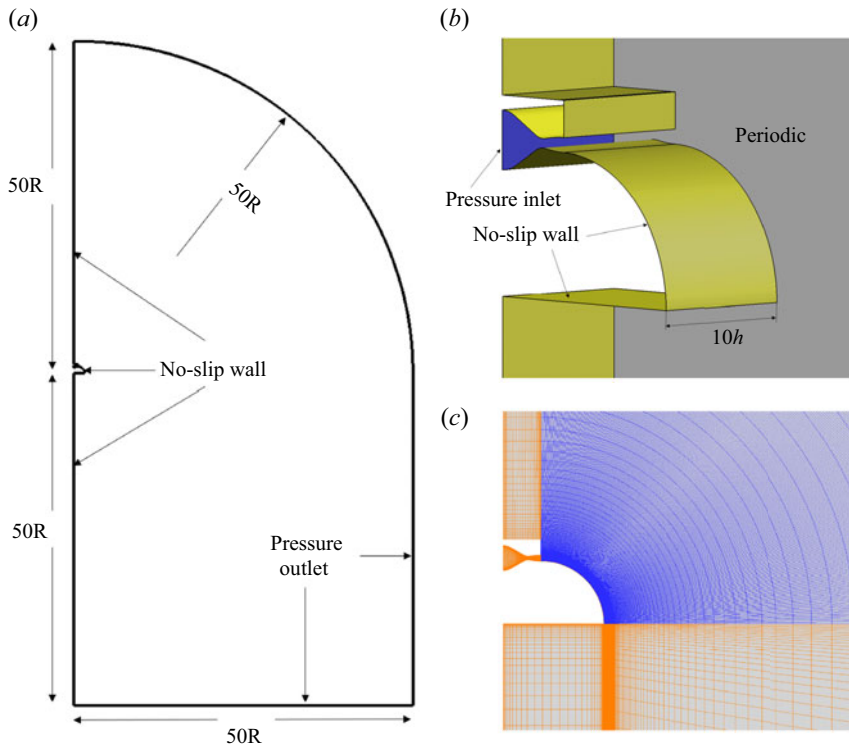
(*a*)

(*b*)

(*c*)

Figure 2. Schematics of (*a*,*b*) computational domain and boundary conditions, and (*c*) grid around the curved wall.

spanwise direction. The inlet of the jet plenum is set to be the pressure inlet, where the nozzle pressure ratio is specified ($p/p_{amb} = NPR$, $T/T_{amb} = 1.2$).

3.2. *Code validation and grid sensitivity*

3.2.1. *Code validation*

A rectangular convergent–divergent nozzle flow (Behrouzi & McGuirk 2009) is presented for the solver validation. The nozzle had inlet, throat and nozzle exit heights of 25.0, 13.1 and 15.75 mm. The axial lengths of the convergent–divergent are 56.6 mm and 55.78 mm, respectively. The nozzle width remains constant at 91.6 mm. The nozzle exit lip thickness is chosen to be 1 mm. The throat hydraulic diameter ($D_h = 22.92$ mm) is chosen as the reference length. The designed nozzle pressure ratio is 4 ($NPR_d = 4.0$, using inviscid approximation without considering the losses and inlet boundary layer effects). Experiments were carried out in the High-Pressure Nozzle Test Facility at Loughborough University (Behrouzi & McGuirk 2009).

The computational grid is similar to that of the LES simulation of Wang & Mcguirk (2013) on the same configuration. There are $201 \times 56 \times 101$ points on the major and minor axes at the nozzle exit in this study. The grid near the wall and the shear layer were refined to accurately solve flow structures there. A total 20×10^6 cells was used. The operating condition is an over-expanded $NPR = 2.5$. The converged steady RANS solution is used as the initial of unsteady DDES simulation. A fixed time step of 7.2×10^{-7} s is used for the calculation, and 10 subiterations are required to reduce the residual at each physical
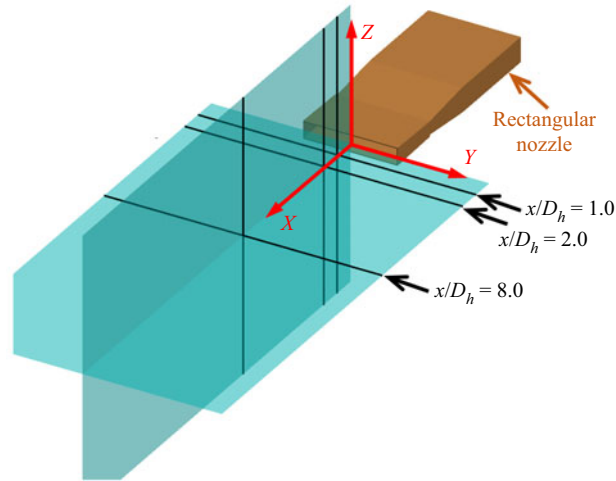
Figure 3. Schematics of the coordinate system and measured stations of Behrouzi & McGuirk (2009)'s experiments.

time step at least two orders of magnitude. The first 10 000 time steps are employed to establish a statistically stationary state, and then statistics are gathered for the additional 10 000 time steps (approximately six solution domain flow through times). Figure 3 shows the schematics of the coordinate system and measured stations of Behrouzi & McGuirk (2009)'s experiments.

Figure 4 shows that the predicted centreline axial velocity profile is consistent with the measured data, which indicates that the solver in this paper can accurately solve the potential core length and the dissipation downstream. Figure 5 shows the comparison between predicted and measured axial velocity profile at three streamwise stations shown in figure 3. Further, the comparison of axes velocity fluctuation root mean square (r.m.s.) is presented in figure 6. All mean velocity and turbulence data are normalized by a reference velocity taken as the centreline axial velocity at nozzle inlet (U_{ref}). The solver utilized in this study could predict the development of the jet shear layer accurately.

3.2.2. *Grid sensitivity*

Two mesh sizes were used to characterize the grid sensitivity of the solution. The coarse mesh contains $N_\theta \times N_y \times N_z = 251 \times 151 \times 121$ grids around the convex surface (resulting in a total of 6.6×10^6 grids), while the fine mesh has $N_\theta \times N_y \times N_z = 301 \times 171 \times 151$ grids around the convex surface (resulting in total 10.5×10^6 grids). The grids in the y-direction are refined near the convex surface and the jet shear layer to accurately trace the boundary layer and the complex vortex development in the shear layer, respectively. In the θ and z directions, the grids are uniformly spaced. The first grid spacing from the convex wall is chosen to ensure that $y^+ < 1$ ($y^+ = \rho_w U_{\tau.w} y_{wall}/\mu_w$, where y_{wall} is the height of the first grid from the wall, $U_{\tau.w}$ is the local friction velocity, ρ_w and μ_w are the local wall density and viscosity).

Figure 7 presents the mean Mach contours for both the coarse and fine grids. The coarse grid results are shown as colour contours, while the fine grid results are shown as solid lines. Figure 8 depicts the ensemble and spanwise averaged streamwise velocity distributions (normalized by ambient air sound speed) at various streamwise locations. Figure 9 shows the jet development along the downstream location by displaying the jet
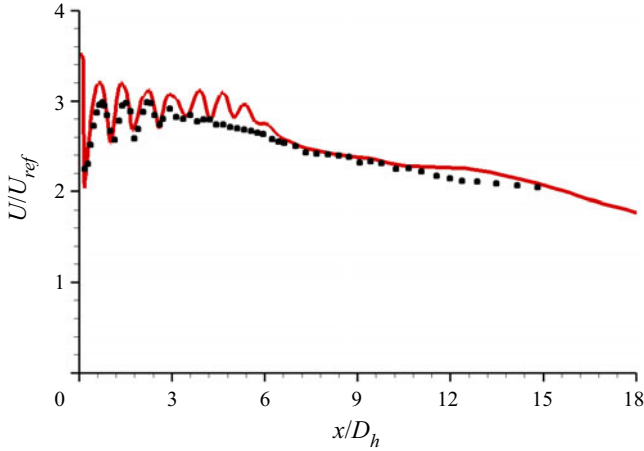
972 A2-8

Figure 4. Comparison between predicted and measured centreline axial velocity profile. Symbols: measured data of Behrouzi & McGuirk (2009); lines: DDES.
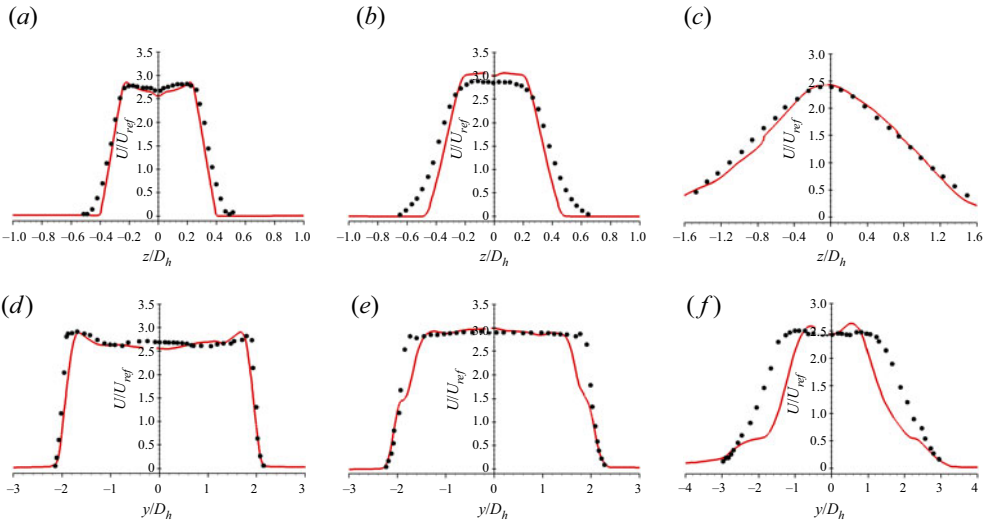

Figure 5. Comparison between predicted and measured minor (*a–c*) and major (*d–f*) axes velocity profile. Symbols: measured data of Behrouzi & McGuirk (2009); lines: DDES. Here (*a*) $x/D_h = 1.0$, (*b*) $x/D_h = 2.0$, (*c*) $x/D_h = 8.0$, (*d*) $x/D_h = 1.0$, (*e*) $x/D_h = 2.0$, (*f*) $x/D_h = 8.0$.
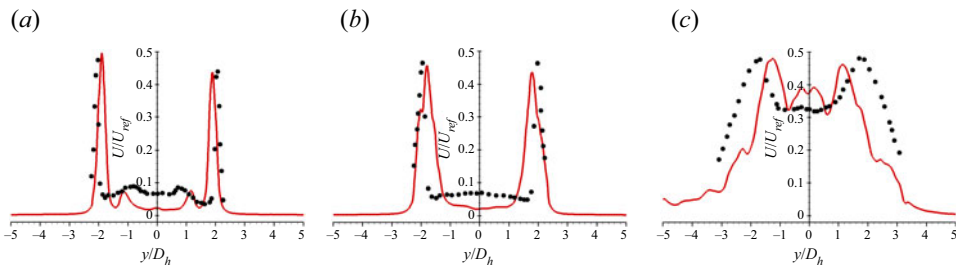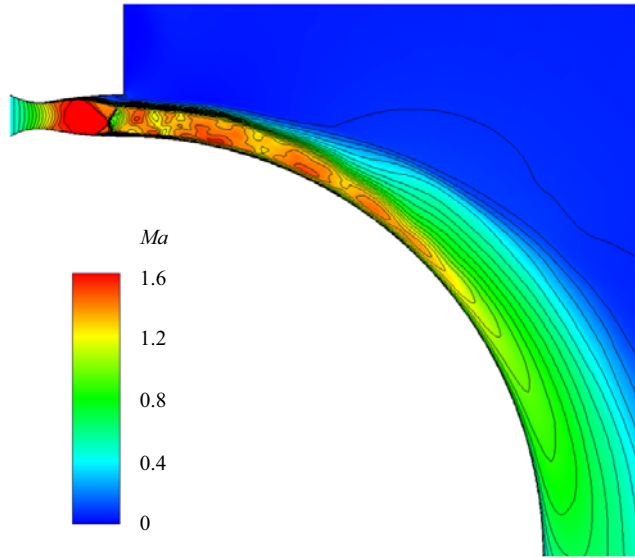

Figure 6. Comparison between predicted and measured major r.m.s. of axes velocity fluctuation. Symbols: measured data of Behrouzi & McGuirk (2009); lines: DDES. Here (*a*) $x/D_h = 1.0$, (*b*) $x/D_h = 2.0$, (*c*) $x/D_h = 8.0$.

Figure 7. Grid resolution on mean flow structure: coarse grid, colour contours; fine grid, black lines.
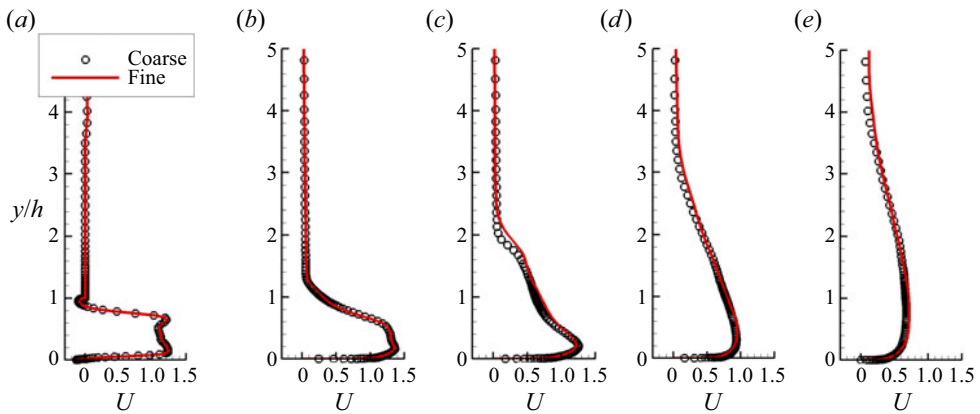
Figure 8. Ensemble and spanwise averaged streamwise velocity distribution from $\theta = 0°$ to $90°$: (*a*) $0°$; (*b*) $25°$; (*c*) $45°$; (*d*) $65°$; (*e*) $90°$.

half-width and vorticity thickness of the shear layer. The results obtained with the two meshes demonstrate excellent grid independence.

Here, the jet half-width (y_2) is the wall normal location where the streamwise velocity is half of its maximum value ($0.5U_{max}$). It is widely used as a measure of the jet thickness in the wall jet literature. While the vorticity thickness (δ_ω) is a popularly used indicator for mixing layer thickness in numerical simulations. It should be noted that the original vorticity thickness formula is $\delta_\omega = \Delta U / |\mathrm{d}u/\mathrm{d}y|_{max}$. The formula is defined in the plane mixing layer. Different from the plane mixing layer, the mainstream velocity of the jet over a convex wall changes significantly as the jet develops downstream (figure 7). Therefore, to consider the effect of the velocity variation, ΔU is calculated by the local maximum streamwise velocity in this study.
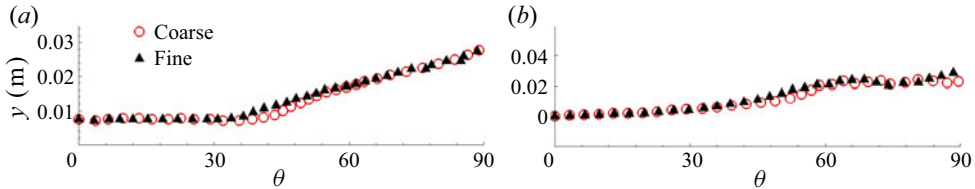
972 A2-10

Figure 9. Ensemble and spanwise averaged (*a*) jet half-width, (*b*) vorticity thickness of the jet shear layer.
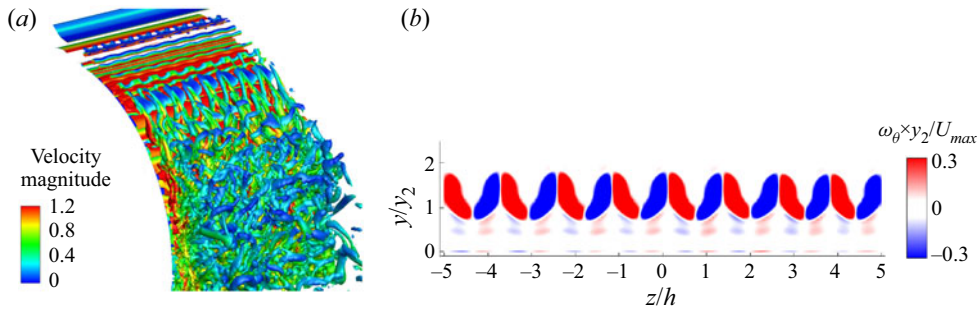

Figure 10. Spanwise flow structure resolution, (*a*) instantaneous visualization of vortex structures using *Q*-criteria ($Q = 100$), (*b*) ensemble averaged streamwise vorticity at $\theta = 25°$.

In addition, the grid independence of the fine mesh will be demonstrated by the following three aspects.

(1) For reliable DDES simulations, the grid size has to be adequately small to resolve the desired turbulent structures. The smallest Kolmogorov scale $\eta = (\nu^3/\varepsilon)^{1/4}$ is estimated approximately 0.04 mm in the jet mixing layer centre for the present simulations, here ν and ε are the kinematic viscosity (calculated by Sutherland's law) and turbulent kinetic energy dissipation rate (estimated by the *RNGk − ε* model), respectively. The grid spacings around the jet mixing layer in the (θ, y, z) directions are specified as (0.52, 0.05, 0.67) mm, which are approximately (12.5, 1.25, 17) times the Kolmogorov scale and are fine enough to resolve the jet mixing layer.

(2) The computation domain in the z direction should be sufficiently wide to capture enough spanwise flow structures. The instantaneous visualization of vortex structures using *Q*-criteria and ensemble average of streamwise vorticity at $\theta = 25°$ are shown in figure 10. It can be seen that the spanwise flow periodicity is well captured and the spanwise scale in the present simulation is reasonable.

(3) The numerical pressure coefficient distribution on the Coanda wall agrees with the experiment of Llopis-Pascual (2017) well (figure 11). This further proves the accuracy of the grid and solver in the present study. Thus, the resolution of the fine mesh is considered to be sufficient for the unsteady numerical simulation and will be utilized in all the present investigations.

For the configuration with protrusions at the nozzle lip (called a forced jet), there is a grid distribution in the streamwise and the wall normal direction similar to the device without protrusions at the nozzle lip (called an unforced jet). In the spanwise direction, the grid near around the protrusions is refined to capture the flow around them. However, the maximum spanwise spacing is consistent with the uniform spacing of the unforced jet.
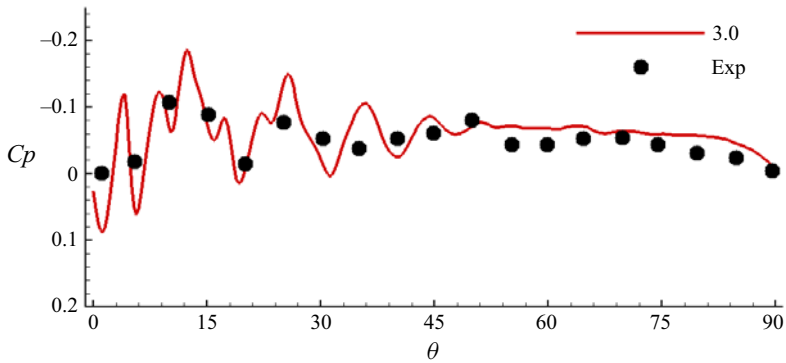
Figure 11. Comparison of pressure coefficient along the Coanda surface of *NPR* = 3.0. Symbols: experiment results of Llopis-Pascual (2017); line: DDES.
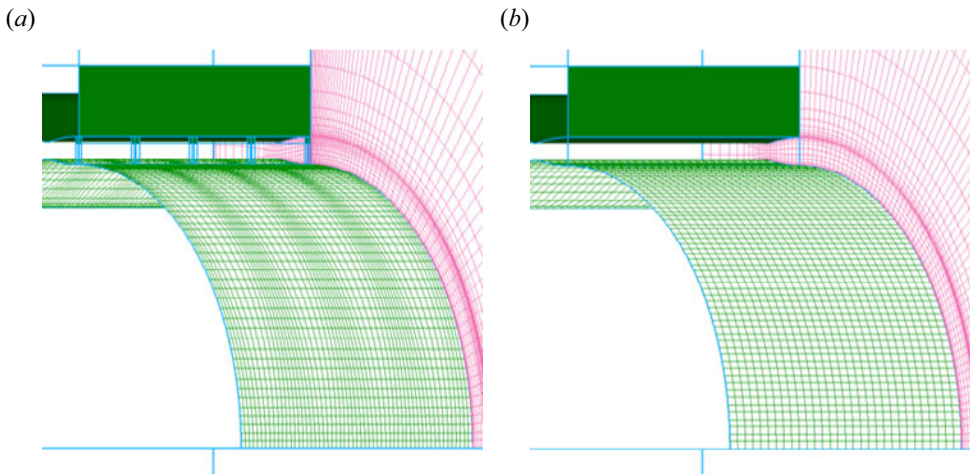

Figure 12. Surface grids display every five grid points: (*a*) forced jet; (*b*) unforced jet.

The mesh contains $N_\theta \times N_y \times N_z = 301 \times 185 \times 281$ grids around the convex surface, resulting in a total of 22.2×10^6 grids. The diagrams of the computational meshes on the Coanda surface and periodic boundary are shown in figure 12.

4. Results and discussion

The overall purpose of this paper is to study the mixing characteristics and enhancement mechanism of the compressible jet over a convex wall by adopting spanwise heterogeneities at the nozzle lip. The nozzle pressure ratios (*NPR*) are specified as 3.0 and 3.9, resulting in nozzle exit Mach numbers of 1.33 and 1.93, and the corresponding convective Mach numbers of 0.66 and 0.88, respectively. The former one is a moderately compressible condition, whereas the latter is a highly compressible condition according to the compression definition in the planar shear layer literature (Bogdanoff 1983; Papamoschou & Roshko 1988; Sandham 1991; Zhang, Tan & Li 2017). The detailed parameters are listed in table 1. It should be noted that the Mach number (*Ma*), velocity

972 A2-12

	Nozzle inlet		Nozzle exit		
	NPR	T_0/T_{amb}	*Ma*	U (m s^{-1})	M_c
Case 1	3.0	1.2	1.33	428.3	0.64
Case 2	3.9	1.2	1.93	556.0	0.88

Table 1. Detailed parameters of different pressure ratios.

(U) and corresponding convective Mach number (M_c) in this table are characterized using the maximum value at the nozzle exit due to the flow non-uniformity.

4.1. *Basic features of mean flow development*

The device without spanwise heterogeneities is employed as a baseline, which is known as the unforced jet, and the jet with spanwise distributed heterogeneities at the nozzle lip is referred to as the forced jet. The instabilities and compressibility effects on the unforced jet shear layer have been studied in our previous work (Wang *et al.* 2023). The influences of the flow structures in the nozzle, the outlet flow non-uniform, the outlet velocity and the outlet Mach number on the instabilities of the shear layer were evaluated. The results show that the flow structures in the nozzle, the non-uniform outlet flow, the change of outlet velocity, have little impact on the instabilities of the shear layer. The instabilities are dominated by the Mach number changing related to the nozzle pressure ratio.

Figure 13 shows the ensemble averaged vortex structures using Q-criteria of the two unforced jet of *NPR* = 3.0 and 3.9. In the moderately compressible condition *NPR* = 3.0 (figure 13*a*), the streamwise vortices can be observed in the shear layer. According to an analysis of the streamwise vorticity transport equation, our previous work (Wang *et al.* 2023) on the identical configuration and flow condition has revealed that the generation of the streamwise vortices is dominated by the centrifugal instability. The spanwise modulation of the streamwise vortices produces the secondary instability of the shear layer, which leads to the rapid instability and growth of the shear layer. Further, for the compressible flow, the vorticity transport equation is

$$\frac{\partial \omega}{\partial t} + u\nabla\omega = \omega\nabla u + \frac{1}{\rho^2}\nabla\rho \times \nabla p + \nu \times \Delta\omega, \qquad (4.1)$$

where ω is the vorticity, u the flow velocity, p the local pressure, ρ the local density and ν the kinematic viscosity coefficient. The second term on the right-hand side is the baroclinic term related to the compressible effect. Figure 14 shows the streamwise vorticity and the contribution of the corresponding baroclinic term at $\theta = 25°$ of the unforced jet with *NPR* = 3.0. It can be seen that the baroclinic term has an opposite contribution to the streamwise vorticity in the shear layer, which indicates that the compressibility has the suppression effect on the streamwise vortices. When the convective Mach number increases to 0.88, as shown in figure 13(*b*), the generation of large-scale streamwise vortices and the growth of the shear layer are considerably inhibited by the highly compressibility effect.

Furthermore, to evaluate the influence of setting heterogeneities at the nozzle lip, figure 15 shows the ensemble and spanwise averaged Mach contours of different pressure ratios. In these figures, the cylinder Coanda surface has been unfurled into abscissa, that is, the x axis represents the streamwise direction and the corresponding coordinate
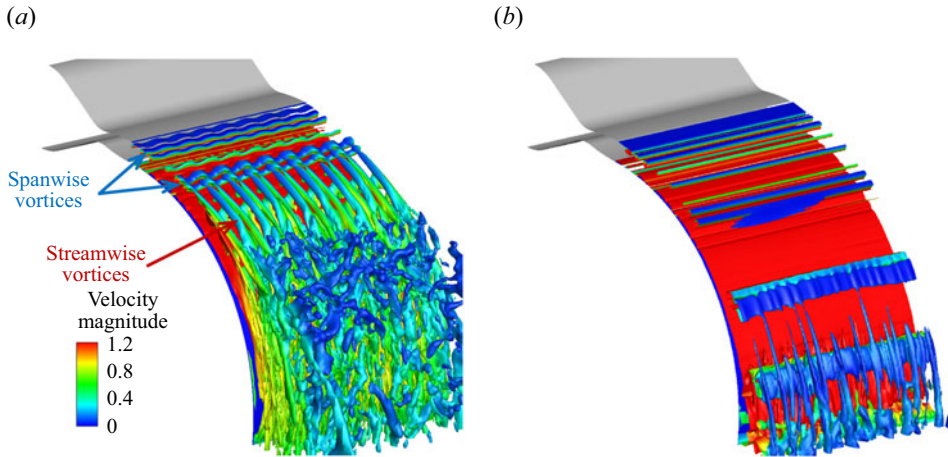
(*a*)   (*b*)

Figure 13. Ensemble averaged vortex structures of the unforced jet using Q-criteria ($Q = 100$, coloured by velocity magnitude): (*a*) $NPR = 3.0$, $M_c = 0.64$; (*b*) $NPR = 3.9$, $M_c = 0.88$.
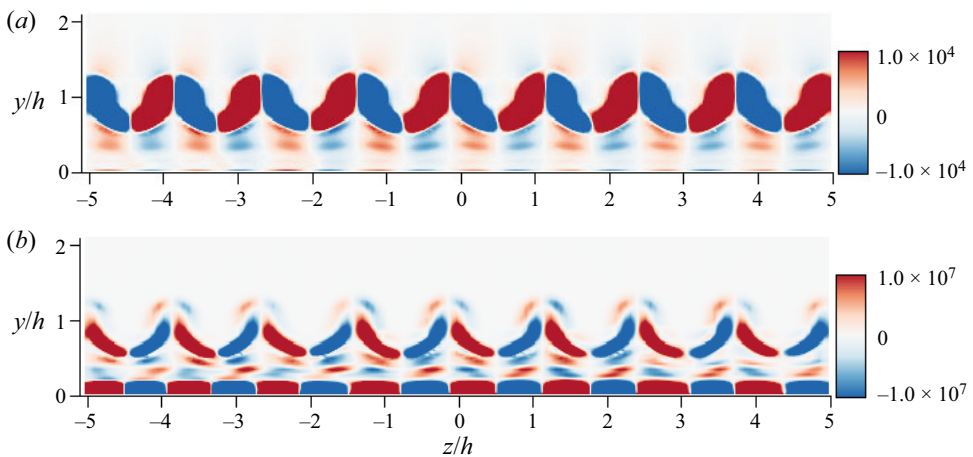
Figure 14. (*a*) Streamwise vorticity, and (*b*) streamwise vorticity arising from the baroclinic term at $\theta = 25°$ (unforced jet, $NPR = 3.0$).

value are the azimuth angle of the cylindrical surface from the nozzle exit. Similarly, the ordinate in the figure corresponds to the radial distance from the cylinder surface and has been normalized by the nozzle exit height. For the moderately compressible situation (figure 15*a,b*), the streamwise vortices induced by centrifugal instability in the unforced jet can destabilize the shear layer rapidly (figure 13*a*). However, the present of spanwise heterogeneities in the forced jet increases the scope of the shear layer to some extent. In terms of the highly compressible condition (figure 15*c,d*), the streamwise vortices in the unforced jet are suppressed (figure 13*b*), which results in a limited growth rate of the shear layer. Once the spanwise distributed protrusions are introduced into the flow, the mixing characteristic of the shear layer is significantly enhanced, that is, the momentum exchange ability is enhanced. The high momentum exchange between the inner and outer sides of the shear layer causes the mainstream velocity of the jet to decrease rapidly, whereas the action region of the shear layer grows significantly.

972 A2-14

(*a*)
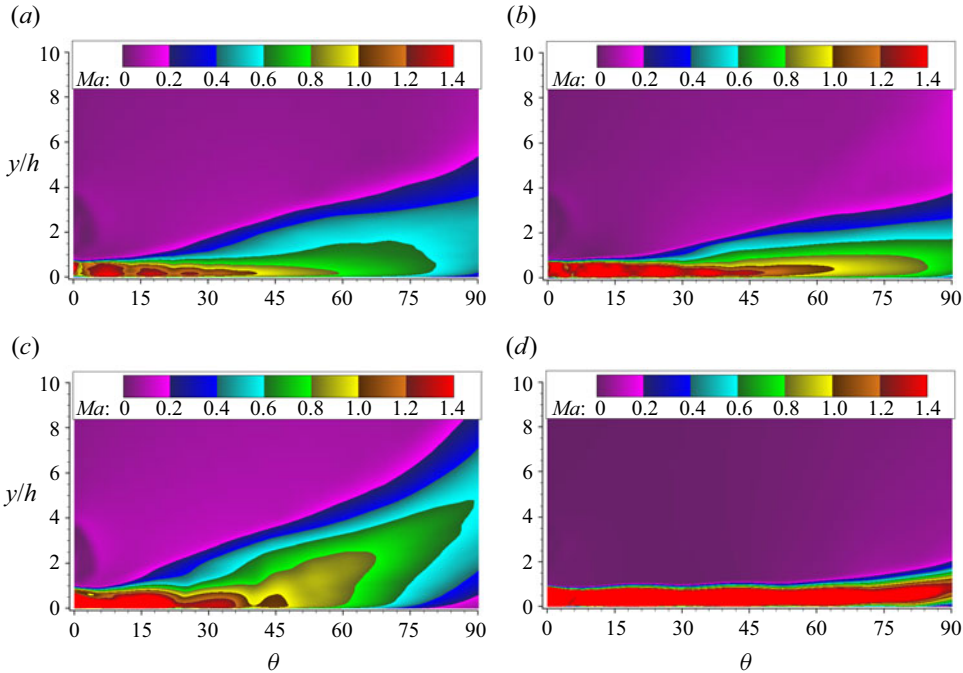

(*b*)

(*c*)

(*d*)

Figure 15. Ensemble and spanwise averaged Mach contours comparison between forced and unforced jet: (*a*) $NPR = 3.0$, $M_c = 0.64$ forced jet; (*b*) $NPR = 3.0$, $M_c = 0.64$ unforced jet; (*c*) $NPR = 3.9$, $M_c = 0.88$ forced jet; (*d*) $NPR = 3.9$, $M_c = 0.88$ unforced jet.
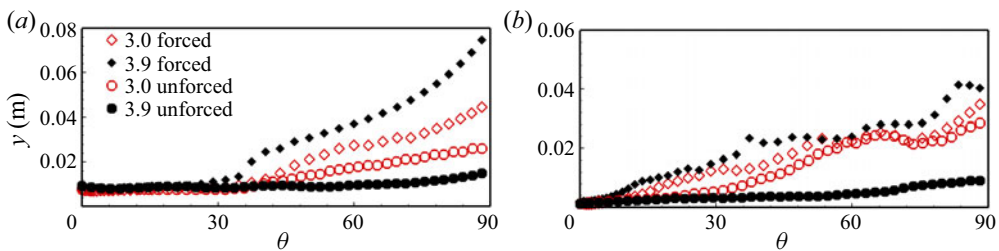
(*a*)

(*b*)

Figure 16. Ensemble and spanwise averaged (*a*) jet half-width, and (*b*) vorticity thickness of the shear layer along the streamwise direction.

In order to quantitively evaluate the development of the unforced and forced jet, figure 16 presents the development of the jet half-width and the shear layer vorticity thickness along the streamwise direction. Compared with the unforced jet, the jet half-width and shear layer vorticity thickness of the forced jet are thickened, indicating that the mixing capacity of the jet shear layer is enhanced. In addition, the location where the jet width and shear layer vorticity thickness begin to grow rapidly advances, suggesting that the shear layer instability has been advanced. This will be further discussed in § 4.2.3.

Another prominent feature can be seen in figure 16 is that the mixing enhancement in the highly compressible state $NPR = 3.9$ is greater than that in the moderately compressible state $NPR = 3.0$. This could be explained by the following two aspects. On the one hand, as compared with the highly compressible condition, the shear layer instability induced by centrifugal instability in the unforced jet is already rather rapid, which leads to a relatively limiting mixing enhancement control effect. On the other hand, a more important
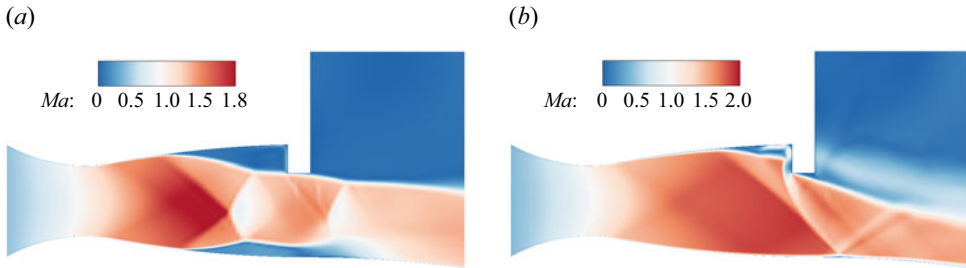
(*a*)   (*b*)

Figure 17. Ensemble averaged Mach contours of the forced jet near the nozzle exit:
(*a*) $NPR = 3.0$, $M_c = 0.64$; (*b*) $NPR = 3.9$, $M_c = 0.88$.

aspect is that the jet studied in this paper works in an over expansion state, and there are separations near the nozzle exit. As shown in figure 17, for the moderately compressible state $NPR = 3.0$, the spanwise distributed protrusions are almost located in the separation region. In comparison, as the pressure ratio increases, the over expansion characteristics of the jet are improved. Consequently, the shock waves in the nozzle are pushed outward, and the associated separation becomes smaller. This enhances the influence of the protrusions on the flow field, thereby increasing the control effect of the mixing enhancement.

4.2. *Mechanism of mixing enhancement*

4.2.1. *Streamwise vorticity in the shear layer*

Due to the influence of compressibility, the generation of streamwise vortices in the highly compressible state are suppressed in the unforced jet (figure 13*b*). However, figure 18 shows the ensemble averaged streamwise velocity development of the forced jet along the streamwise direction. The spanwise distributed protrusions would induce initial instability in the shear layer. This initial instability is subsequently maintained and amplified. In fact, Han *et al.* (2006) found that similar forcing at the nozzle lip in a plane wall jet did not result in streamwise vortices due to the absence of the centrifugal effects to sustain them. It suggests that the centrifugal effect would be responsible for the amplified initial disturbance.

The mean vorticity transport equation provides a budget of the various effects contributing to a change in the mean vorticity. For a given streamwise location ($\theta = $ const.), mean streamwise vorticity arising from the centrifugal effects in a mean term, $CFG(1) = (1/r)(\partial u_\theta^2/\partial z)$, which is combined with the results of the skewness effect, $\langle\omega_r\rangle(\partial\langle u_\theta\rangle/\partial r) + \langle\omega_z\rangle(\partial\langle u_\theta\rangle/\partial z)$, and the curvature effect, $-\langle u_\theta\rangle\langle\omega_r\rangle/r$. Similarly, the turbulent term, $CFG(2) = (1/r)(\partial u_\theta'^2/\partial z)$, accounts for the mean vorticity arising from the turbulent stresses in the flow. Figure 19 shows the ensemble averaged streamwise vorticity at $\theta = 45°$. The contours of the centrifugal effects in a mean term (figure 19*b*) show good correspondence with the streamwise vorticity contours (figure 19*a*), which suggests that the centrifugal effect dominants the streamwise vorticity production. For the centrifugal terms arising from the turbulent stresses (figure 19*c*), it has a pair of opposite vortices at the position of each streamwise vorticity cell, which would lead to the radial distribution of the streamwise vorticity shifting away from the wall. However, the contribution of this term is one order of magnitude smaller than that of the mean term.

A further insight into figure 19(*a*) is that the transportation effect of streamwise vortices produces alternating upwash and downwash regions. This spanwise modulation would trigger the inflection instability of the spanwise flow. The spanwise modulation and
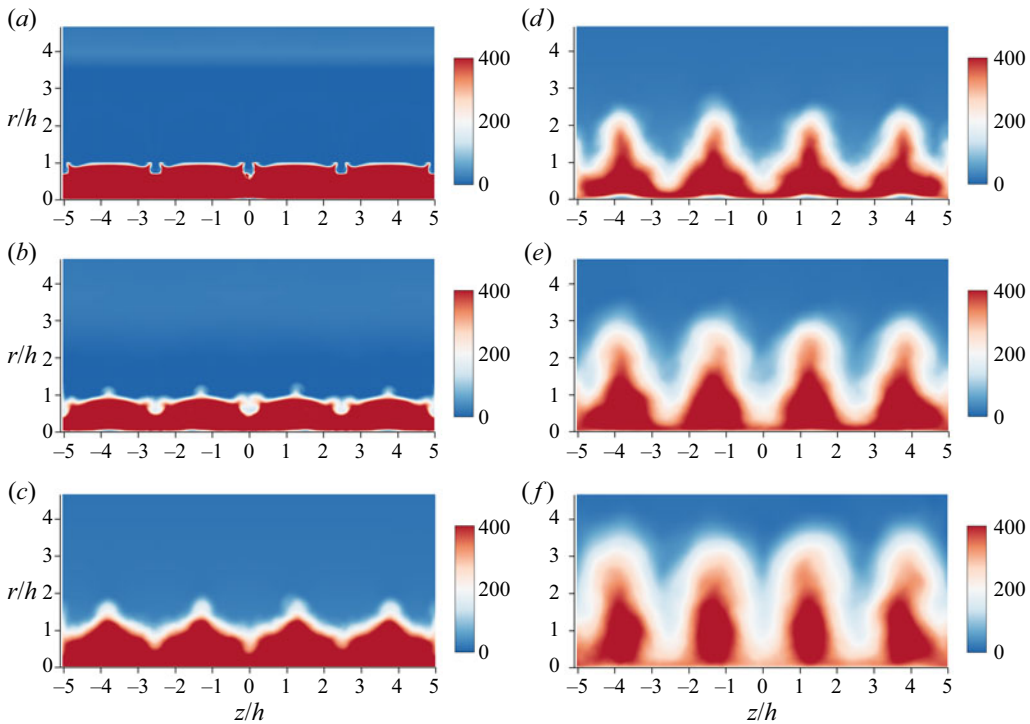
972 A2-16

Figure 18. Ensemble averaged streamwise velocity development along azimuth angles ($NPR = 3.9$, forced jet): (*a*) $\theta = 0°$; (*b*) $\theta = 5°$; (*c*) $\theta = 15°$; (*d*) $\theta = 25°$; (*e*) $\theta = 35°$; (*f*) $\theta = 45°$.

associated secondary instabilities lead to the mixing enhancement in a forced jet, which will be discussed in detail in § 4.2.3.

4.2.2. *Spanwise wavelength of the streamwise vorticity*

In both an unforced and a forced incompressible jet over a convex wall, previous studies have found that the spanwise wavelength scales as twice the local jet half-width (Likhachev *et al.* 2001; Han *et al.* 2006; Pandey & Gregory 2020, 2021). As the jet streams downstream and the jet width increases, this relationship is maintained through the streamwise vortex pair merging process. However, the study of Wang *et al.* (2023) on an unforced compressible convex wall jet indicated that in addition to the convection, diffusion and breaking of the streamwise vortices, no merging process of vortex pairs was observed with the development of jet as well as the increase of jet half-width. In terms of the forced jet here, in order to observe the flow development along the streamwise direction, figure 20 shows the streamwise vorticity, streamwise velocity and radial velocity contours of the stream-span plane $y/h = 1$. The streamwise streaks are caused by the streamwise vortices associated with the centrifugal instability. In the forced jet, the merging phenomenon of the streamwise vortex pair is also not observed. The spanwise wavelength is maintained at a constant value as the forcing wavelength at the nozzle lip, until it breaks into smaller vortices.

Figure 21 shows the streamwise vortices' distributions in different cross-stream locations. Like the unforced jet, the forced jet is spanwise periodic. Unlike the unforced jet, the spanwise wavelength of the forced jet is consistent with the spanwise distributed
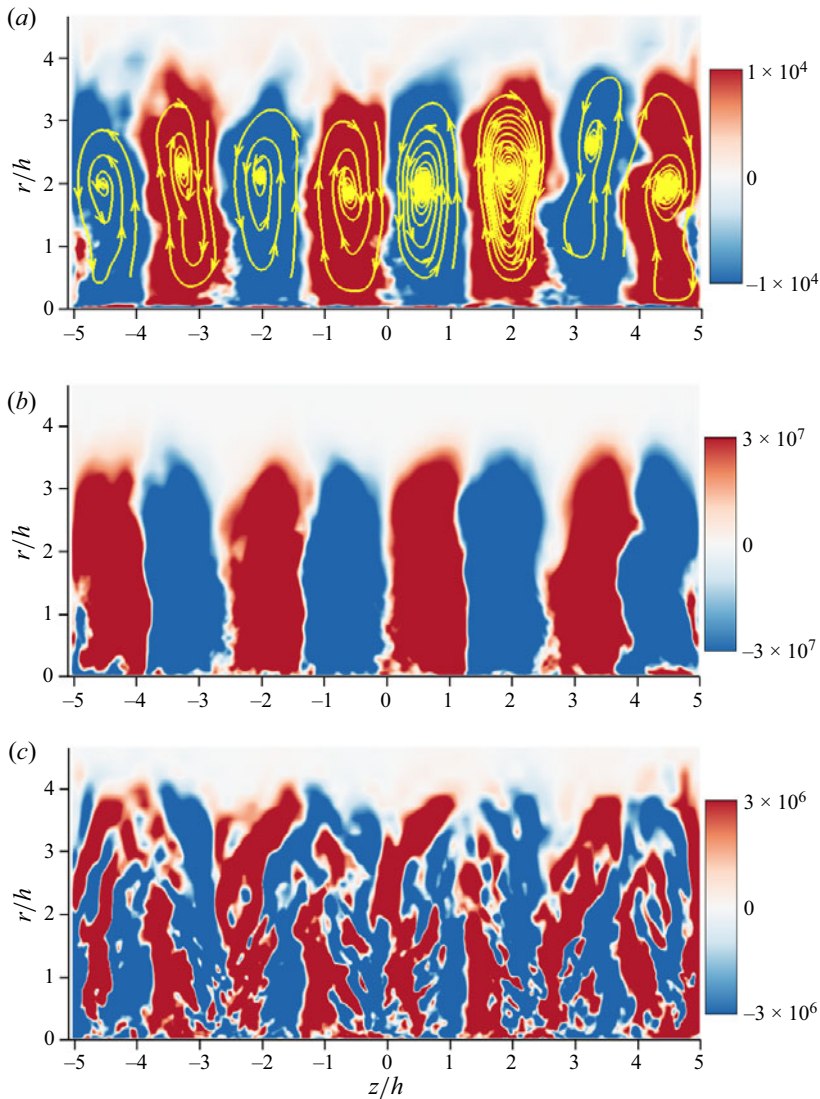
Figure 19. Ensemble averaged streamwise vorticity at $\theta = 45°$ ($NPR = 3.9$, forced jet): (*a*) streamwise vorticity (ω_θ) contours and streamlines; (*b*) streamwise vorticity due to centrifugal terms arising from the mean flow ($CFG(1)$); (*c*) streamwise vorticity due to centrifugal terms arising from the turbulent stresses ($CFG(2)$).

forced excitation at the nozzle lip, which is approximately twice the spanwise wavelength of the unforced jet. In addition, the streamwise vortices of the forced jet are stronger and have a wider range of action, especially in the radial direction.

4.2.3. *Streamwise travelling wave*
In the boundary layer stability studies (Andersson *et al.* 2001; Schlatter *et al.* 2008; Konishi & Asai 2010), the amplitude growth of elongated streamwise streaks due to the lift-up mechanism can develop instabilities. This instability of the streamwise streaks is referred as a secondary instability, which induces the meandering motion of the
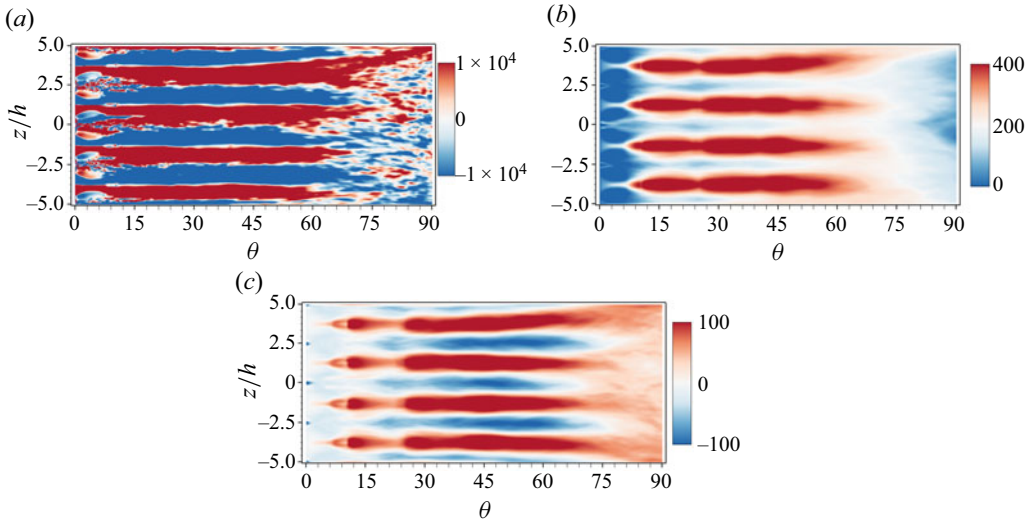
Figure 20. Ensemble averaged contours of stream-span plane at $y/h = 1$ (*NPR* = 3.9, forced jet):
(*a*) streamwise vorticity (ω_θ), (*b*) streamwise velocity (U), (*c*) radial velocity (V).
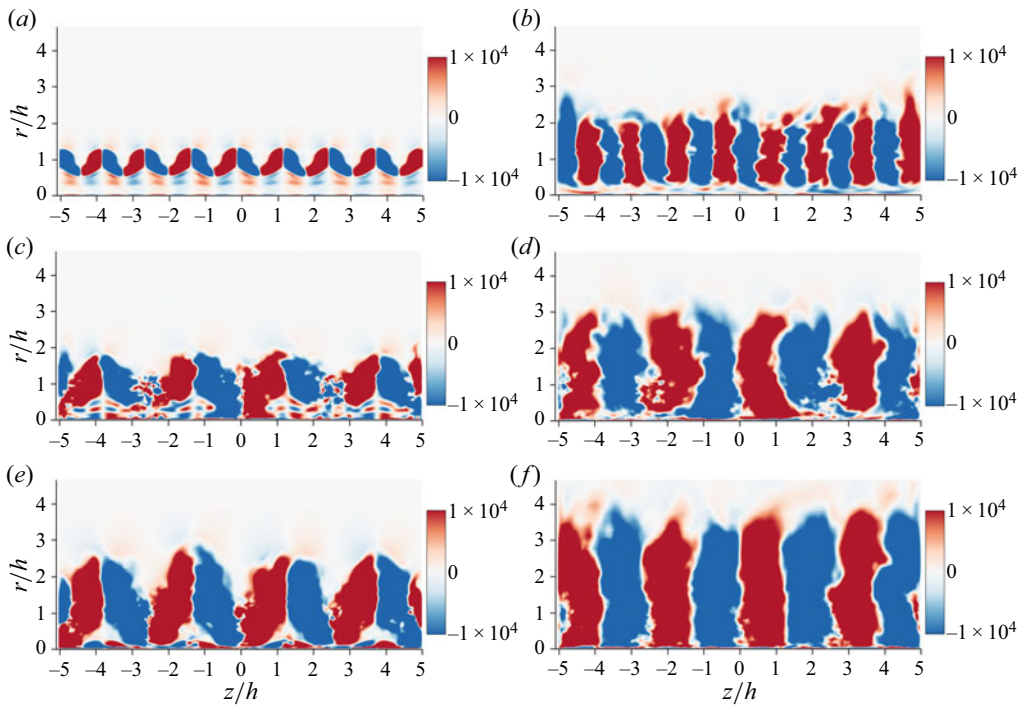

Figure 21. Ensemble averaged streamwise vorticity contours at $\theta = 25^\circ$ (*a,c,e*), and $\theta = 45^\circ$ (*b,d,f*). Here
(*a,b*) *NPR* = 3.0, unforced jet, (*c,d*) *NPR* = 3.0, forced jet, (*e,f*) *NPR* = 3.9, forced jet.
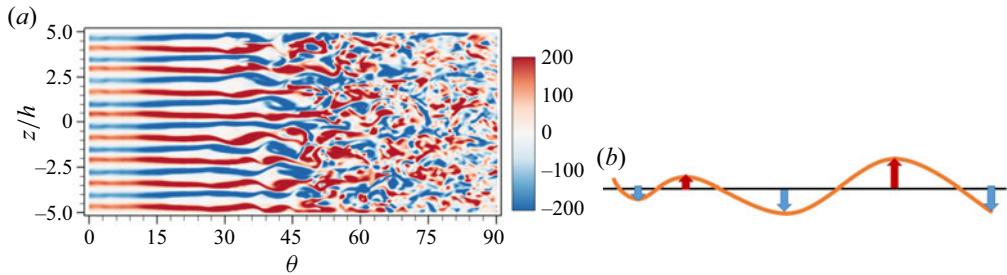
(*a*)

Figure 22. (*a*) Instantaneous streamwise vorticity contours at stream-span plane ($y/h = 0.8$, (unforced jet, $NPR = 3.0$)), and (*b*) schematic of a streamwise travelling sinuous wave.

streamwise vortices. The convection of spanwise meandering motion in the streamwise direction behaves as a streamwise travelling wave. There are four possible modes in this travelling wave including the fundamental sinuous mode, subharmonic sinuous mode, fundamental varicose mode and subharmonic varicose mode (figure 2 in Andersson *et al.* (2001)). In the subharmonic cases, sinuous (varicose) fluctuations of the low-speed streaks are always associated with staggered varicose (sinuous) oscillations of the high-speed streaks. The secondary instabilities are also expected to be active in the shear layer of the convex wall jet. In an incompressible convex wall jet, Pandey & Gregory (2020) revealed the existence of a travelling wave by carrying out POD analysis in the downwash region between two counter-rotating vortices. The conditional averaged results showed that this travelling wave was most consistent with the descriptions of a subharmonic sinuous mode in the boundary layer literature. They also found that the subharmonic sinuous instability is dominant in the incompressible convex wall jet.

In the compressible convex wall jet studied here, figure 22(*a*) shows the instantaneous streamwise vorticity contours of the unforced moderately compressible case $NPR = 3.0$. The spanwise meandering motion of the streamwise vortices can be clearly observed. This meandering characteristic indicates the presence of streamwise travelling waves in the shear layer. Figure 22(*b*) shows the schematic of a streamwise travelling sinuous wave. As the wave convects downstream, alternating positive and negative spanwise fluctuation regions are induced. Furthermore, POD analysis is applied to the snapshots of the stream-radial section in the upwash region. Figure 23 presents the eigenvalues (energy) distributions of the POD modes. It is notable that the first two modes have nearly the same eigenvalues. This degeneracy of eigenvalues (eigenvalue pairs) has been demonstrated to be caused by the spatiotemporal symmetries of the flow field (Deane *et al.* 1991; Pandey & Gregory 2020). Further, spatial distributions of the first two POD modes shown in figure 24 appear virtually as phase-shifted versions of each other, which confirms the presence of the travelling wave. The mode spatial backward tilted pattern is due to the fact that the inner part of the jet flows faster than the outer side. It should be noted that the cylinder Coanda surface has been unfurled into abscissa in these figures.

In terms of the forced jet, the spanwise distributed protuberances at the nozzle lip were used to force the initial disturbances and subsequently sustained by the centrifugal effects. The above POD analysis was repeated at two other forced conditions of $NPR = 3.0$ and $NPR = 3.9$ that correspond to convective Mach numbers of $M_c = 0.66$ and $M_c = 0.88$, respectively. Figure 25 shows the eigenvalues (energy) distributions of the POD modes for each forced state. Compared with the unforced jet (figure 23), the eigenvalues of the first two modes are farther apart, which means that the spatiotemporal symmetry of the forced
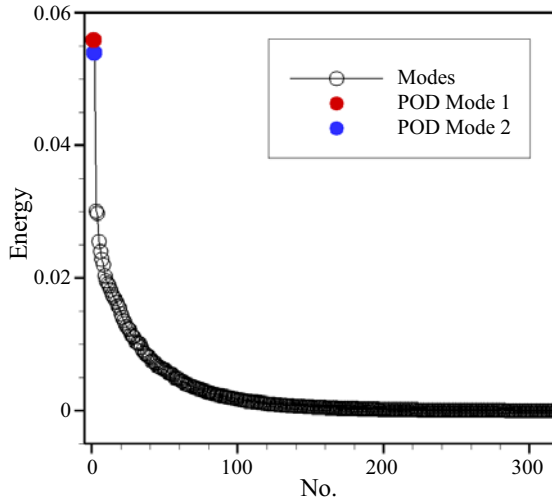
Figure 23. The POD analysis for the spanwise velocity fluctuation of upwash region, POD modes ranked as their eigenvalue (energy) (unforced jet, $NPR = 3.0$).
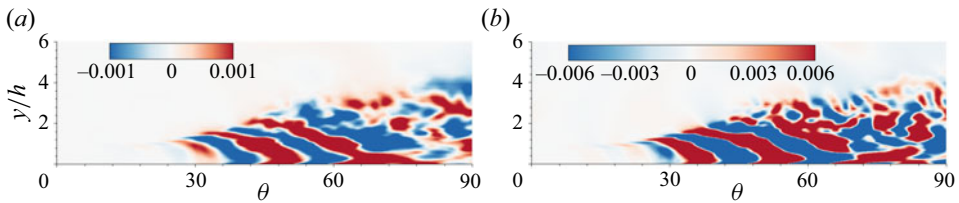

Figure 24. Spatial distributions of the first two POD modes ($NPR = 3.0$, unforced jet): (*a*) mode 1; (*b*) mode 2.
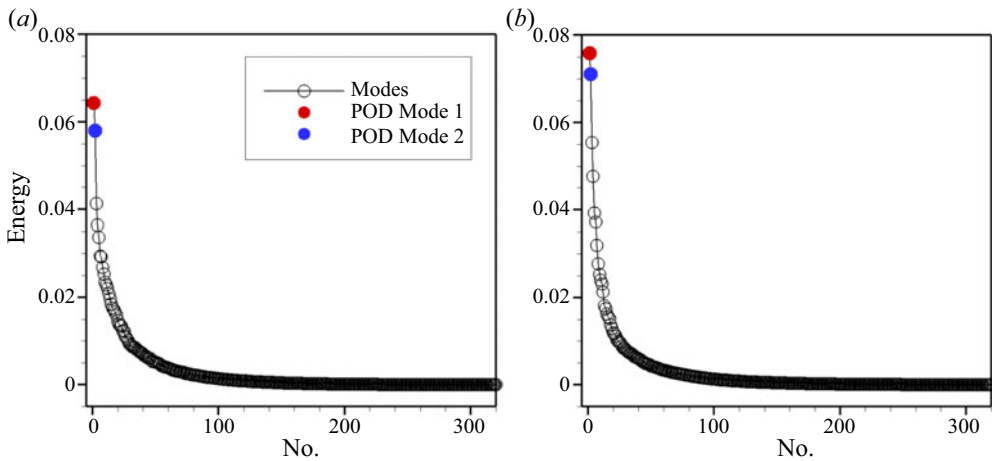

Figure 25. POD analysis for the spanwise velocity fluctuation of upwash region. POD modes ranked as their eigenvalue (energy): (*a*) $NPR = 3.0$, forced jet; (*b*) $NPR = 3.9$, forced jet.
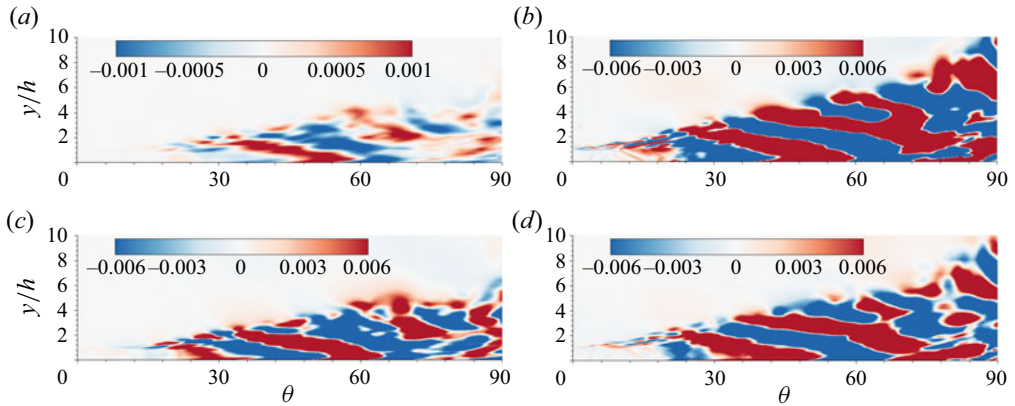
Figure 26. Spatial distributions of the first two POD modes: (*a*) mode 1 (*NPR* = 3.0, forced jet); (*b*) mode 1 (*NPR* = 3.9, forced jet); (*c*) mode 2 (*NPR* = 3.0, forced jet); (*d*) mode 2 (*NPR* = 3.9, forced jet).

flow is broken to some extent. However, the space distributions of the first two modes shown in figure 26 still exhibit streamwise alternating structures. Moreover, the similar and shifted mode shapes in the streamwise direction confirm the existence of travelling waves in the forced jet.

The above POD analysis in the stream-radial section of the upwash region reveals the presence of the travelling wave in both the unforced and forced convex wall jet. However, there are four possible modes in this travelling wave instability (Andersson *et al.* 2001). The POD analysis of spanwise velocity fluctuation in the stream-span plane can provide insights into the identification of specific travelling wave instability modes. Figure 27 shows the eigenvalues (energy) distributions of the POD modes, the degeneracy of the first two POD eigenvalues confirms the existence of the travelling wave. For the unforced jet, figure 28(*a*) shows the mean streamwise velocity contour, which represents spanwise alternating high-speed and low-speed streaks. Figure 28(*b*) shows the spatial distributions of the first POD mode, in which the solid line outlines the sinuous mode instability and the dashed line outlines the varicose mode instability. The varicose type mode is dominated at the early stage of the jet instability, both sinuous and varicose types of disturbances are observed later. It should be noted that even in the same low speed streak, the secondary instability mode may change with the development of the jet. This suggests that there are competitions between different secondary instability modes. In terms of the forced jet, as shown in figure 29, the sinuous type motion seems to dominate due to a sinuous type instability and is more easily excited than the varicose type instability. In fact, Andersson *et al.* (2001) investigated nonlinear evolution of boundary layer streaks, and found that the critical amplitude of the sinuous instability mode is approximately 26 % of the free stream velocity, while varicose waves are more stable and have a critical amplitude of approximately 37 %.

Another salient feature from comparing figures 24 and 26, as well as figures 28(*b*) and 29(*b*), is that the secondary instabilities of the forced jet are excited earlier than those of the unforced jet. In fact, the travelling wave modes of the forced jet are excited near the exit of the jet, while that of the unforced jet does not appear until streamwise location $\theta = 30°$. In other words, the secondary instability of the forced jet acts earlier on the shear layer, leading to a rapid instability of the shear layer and thus enhancing the mixing characteristics.
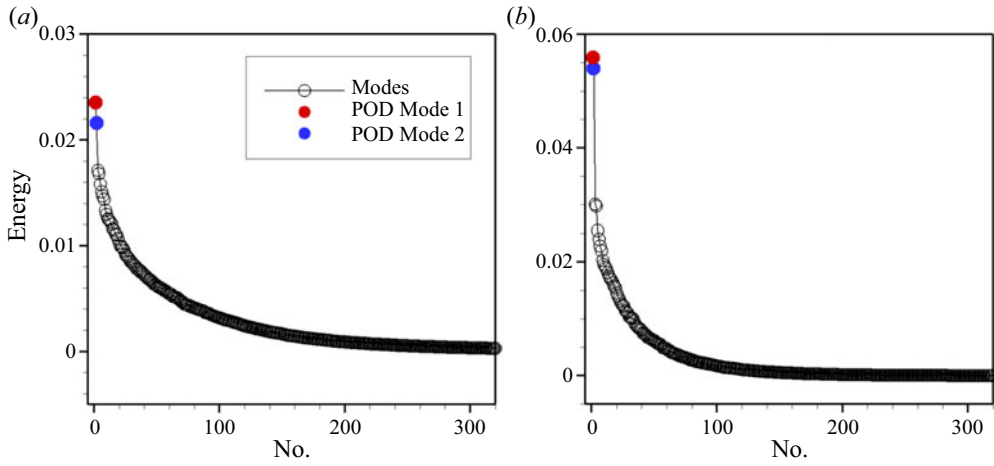
972 A2-22

Figure 27. POD analysis for the spanwise velocity fluctuation of upwash region. POD modes ranked as their eigenvalue (energy): (*a*) *NPR* = 3.9, forced jet; (*b*) *NPR* = 3.0, unforced jet.

Figure 28. (*a*) Mean streamwise velocity contour, (*b*) spatial distributions of the first POD mode, where solid line outlines the sinuous mode instability and dash line outlines the varicose mode instability (*NPR* = 3.0, unforced jet).
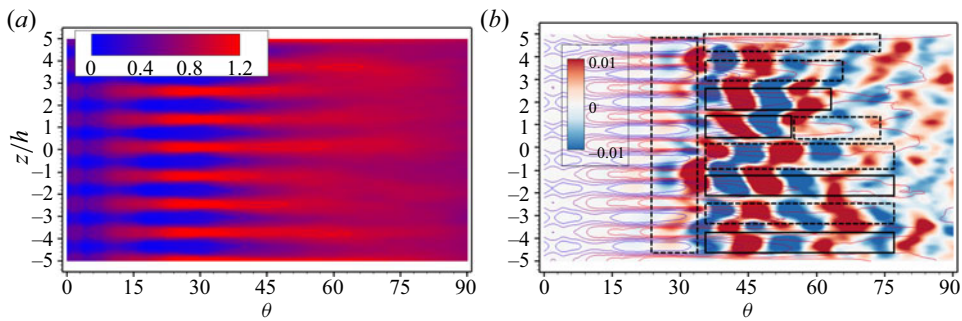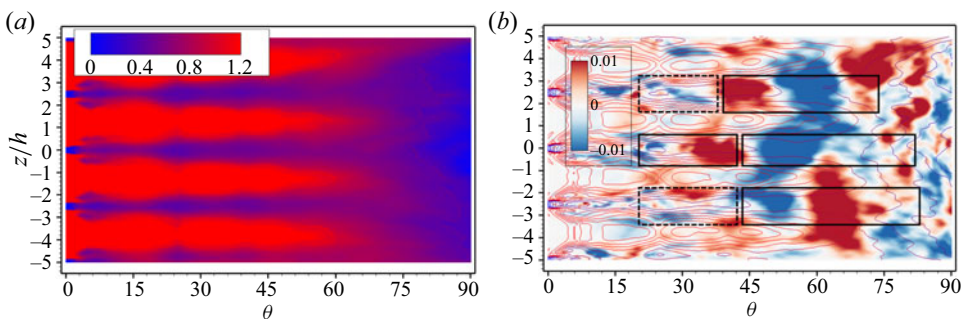

Figure 29. (*a*) Mean streamwise velocity contour, (*b*) spatial distributions of the first POD mode, where solid line outlines the sinuous mode instability and dash line outlines the varicose mode instability (*NPR* = 3.9, forced jet).
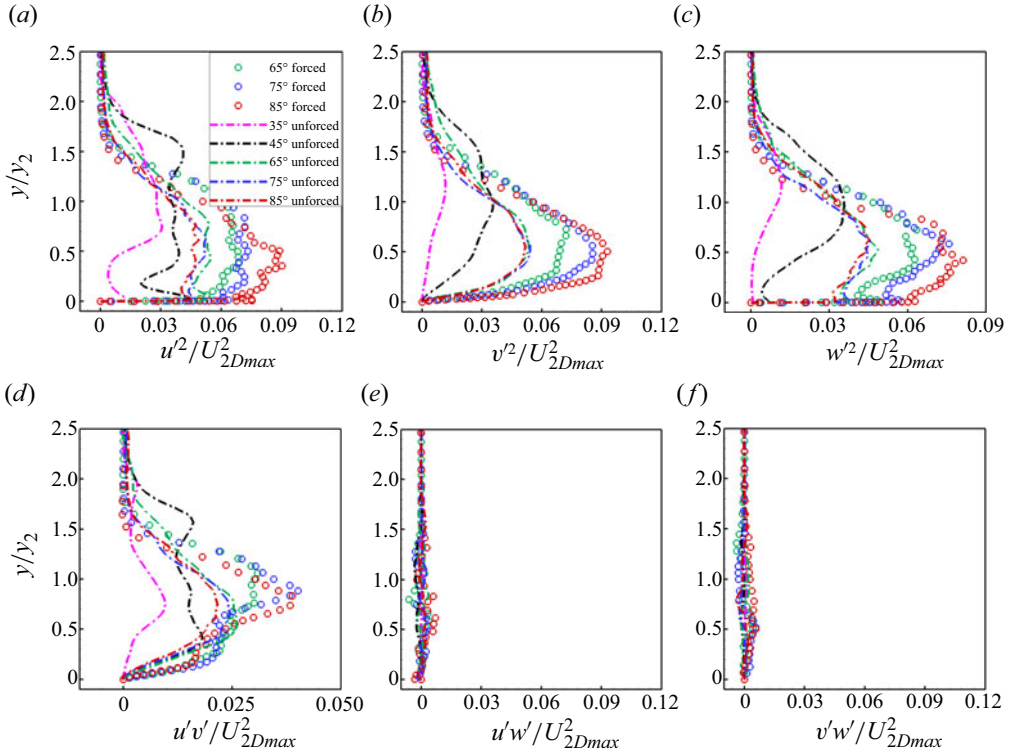
Figure 30. Reynolds stresses development along the streamwise direction ($NPR = 3.0$): (a) $\overline{u'^2}/U_{2Dmax}^2$; (b) $\overline{v'^2}/U_{2Dmax}^2$; (c) $\overline{w'^2}/U_{2Dmax}^2$; (d) $\overline{u'v'}/U_{2Dmax}^2$; (e) $\overline{u'w'}/U_{2Dmax}^2$; (f) $\overline{v'w'}/U_{2Dmax}^2$.

4.3. *Turbulence characteristics*

According to the analyses above, protrusions at the nozzle lip of the forced jet could trigger initial instability in the shear layer. This initial disturbance will be maintained and amplified downstream by the centrifugal effect, leading to stronger streamwise vortices and earlier instability in the shear layer. In this subsection, the turbulence characteristics of both unforced and forced jet are analysed to present mixing enhancement from the perspective of Reynolds stresses. In order to obtain the two-dimensional (2-D) profiles, the stresses are averaged across the spanwise direction. The local jet half-width y_2 and spanwise averaged maximum streamwise velocity U_{2Dmax} are used as the normalization of length scale and velocity scale, respectively.

In the moderately compressible case ($NPR = 3.0$), figure 30 shows the Reynolds stresses 'development along streamwise locations. The shear stresses $\overline{u'w'}$ and $\overline{v'w'}$ are close to zero due to the spanwise average over several wavelengths. For the unforced jet, the Reynolds stresses increase rapidly after $\theta = 30°$, where instabilities are fully excited by streamwise vortices. Then they exhibit self-similar characteristics after $\theta = 60°$, where large scale streamwise vortices break into smaller vortices. However, the turbulence stresses in the forced jet are enhanced due to the stronger streamwise vortices and the earlier secondary instabilities induced by the spanwise distributed heterogeneities at the nozzle lip. The maximum turbulent stresses in the shear layer are approximately twice those of the unforced jet. The radial position of maximum fluctuation is closer to the wall (in the normalized sense) owing to stronger streamwise vortices in the forced jet. In addition,
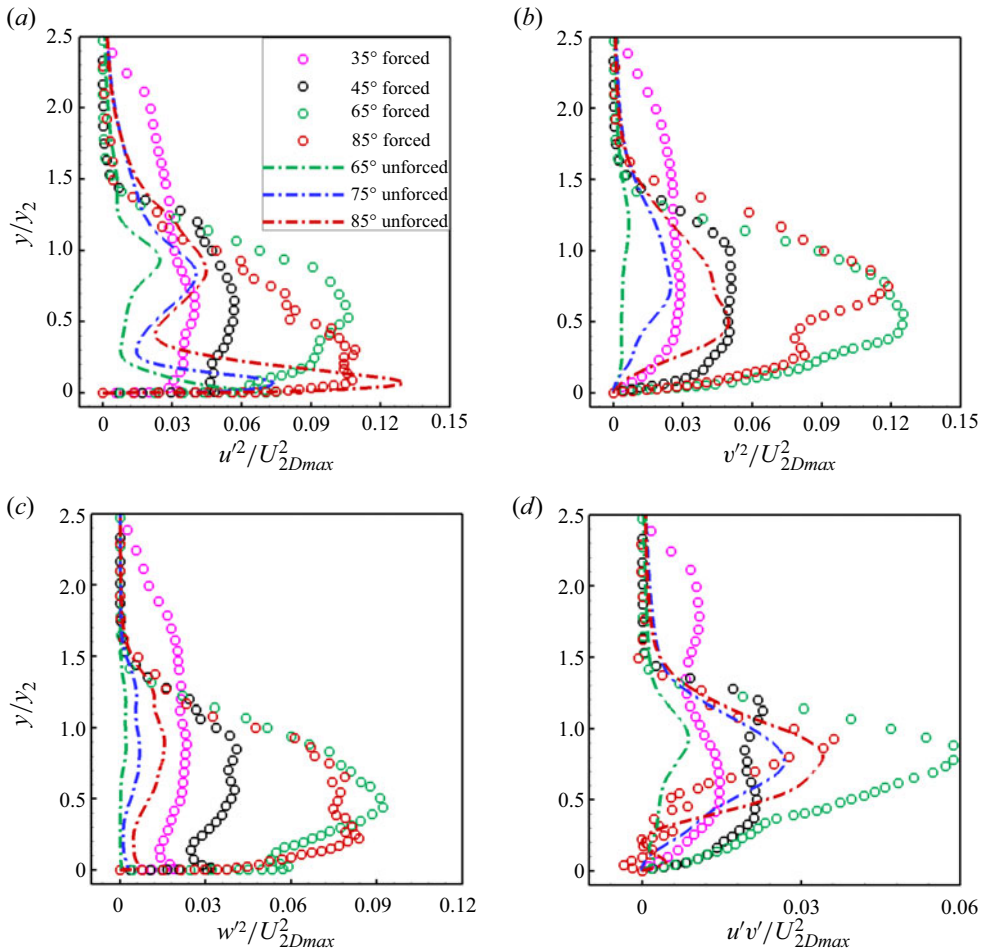
972 A2-24

Figure 31. Reynolds normal stresses development along the streamwise direction ($NPR = 3.9$):
(a) $\overline{u'^2}/U_{2Dmax}^2$; (b) $\overline{v'^2}/U_{2Dmax}^2$; (c) $\overline{w'^2}/U_{2Dmax}^2$; (d) $\overline{u'v'}//U_{2Dmax}^2$.

the enhanced streamwise vortices and associated instabilities in the forced jet make it more difficult to be in equilibrium, resulting in a continued increase in turbulent stresses downstream and do not achieve self-similarity as unforced jet.

The Reynolds stresses development of the highly compressible condition ($NPR = 3.9$) are shown in figure 31. In the unforced jet, large-scale streamwise vortices, which respond to the rapid instability of the shear layer, are significantly inhibited by the high compression effect (Wang *et al.* 2023). The absence of the large-scale streamwise vortices leads to a low intensity turbulence fluctuation in the unforced jet shear layer. Moreover, the spanwise normal stress is more suppressed than the streamwise and radial normal stresses, resulting in turbulence anisotropy. In terms of the forced jet, similar to the moderately compressible case, the stresses here are enhanced as a result of instabilities induced by the spanwise distributed heterogeneities. The enhanced turbulent characteristics tend to be isotropic.

5. Conclusions

In this study, the spanwise distributed heterogeneities at the nozzle lip were employed to achieve mixing enhancement in the compressible convex wall jet. The mixing enhancement characteristics and mechanisms were numerically investigated using the DDES method based on the SST turbulence model. In addition, POD was used to gain further insight into the dynamical behaviours of the flow instability mode. The main conclusions are summarized as follows.

(1) In the highly compressible condition, the development of the mean flow show that the jet half-width and the shear layer vorticity thickness growth rates are significantly increased in the forced jet. This indicates that the mixing as well as the momentum exchange of the shear layer is significantly enhanced by setting spanwise distributed heterogeneities at the nozzle lip.

(2) The analysis of the mean vorticity transport equation reveals that the initial perturbations from the spanwise distributed heterogeneities are maintained and amplified by the centrifugal effect, resulting in forced streamwise vortices in the shear layer. The instabilities induced by the streamwise vortices are responsible for the rapid instability and mixing enhancement in the forced jet.

(3) The development of the streamwise vortices show the convection, diffusion and breaking instead of the merging characteristics. The spanwise wavelength of the streamwise vortices is maintained at a constant value, which is consistent with the spanwise distributed forced excitation, until it breaks into smaller vortices. The forced streamwise vortices are stronger and have a wider range of action than that in the corresponding unforced jet.

(4) The spanwise meandering motion of the streamwise vortices is observed in the instantaneous streamwise vorticity contour of the span-radial section. This meandering characteristic indicates the presence of the streamwise travelling waves. The POD analysis carried out in in the upwash region of the stream-radial section shows that the first two modes have nearly the same eigenvalues. This degeneracy of eigenvalues (eigenvalue pairs) and the phase-shifted spatial distributions of the first two POD modes further confirm the presence of the travelling wave.

(5) The POD analysis carried out in the span-radial section provides further insight into the identification of the specific travelling wave instability modes. In the unforced jet, both sinuous and varicose types of disturbances are observed, there would be competition between different secondary instability modes. In terms of the forced jet, the sinuous type motion is dominated because the sinuous type instability is more easily excited than the varicose type instability.

(6) The turbulence stresses in the forced jet are enhanced due to the stronger streamwise vortices and the earlier secondary instabilities induced by the spanwise distributed heterogeneities. The maximum turbulent stresses in the shear layer are approximately twice those of the unforced jet. In the moderately compressible case, the turbulent stresses exhibit self-similar characteristics after $\theta = 60°$. Whereas the stresses in the forced jet do not achieve self-similarity due to the enhanced streamwise vortices and associated instabilities, which makes the jet more difficult to be in equilibrium. The highly compressibility effect suppresses the spanwise normal stress more than the streamwise and radial normal stresses, resulting in turbulence anisotropy in the unforced jet. In comparison, the enhanced turbulent characteristics of highly compressible condition tend to be isotropic in the forced jet.

Author ORCIDs.

Qing Wang https://orcid.org/0000-0002-5769-5451;

Feng Qu https://orcid.org/0000-0001-8811-0674.

REFERENCES

ALEXANDER, M.G., ANDERS, S.G., JOHNSON, S.K., FLORANCE, J.P. & KELLER, D.F. 2005 Trailing edge blowing on a two-dimensional six-percent thick elliptical circulation control airfoil up to transonic conditions. *NASA Tech. Rep.* TM-2005-213545, Langley Research Center, Hampton, VA, US.

ANDERSSON, P., BRANDT, L., BOTTARO, A. & HENNINGSON, D.S. 2001 On the breakdown of boundary layer streaks. *J. Fluid Mech.* **428**, 29–60.

BEHROUZI, P. & MCGUIRK, J.J. 2009 High speed jet plume experimental study: phase 2/part 1 – RRLU-1 nozzle, full experimental results. In *Dept. of Aero. Auto. Eng. Report TT09R02-A*.

BEVILAQUA, P.M. & LEE, J.D. 1980 Development of a nozzle to improve the turning of supersonic Coanda jets. *Tech. Rep.* AFWAL-TR-80-3027. Flight Dynamics Laboratory, Air Force Wright Aeronautical Laboratories, Air Force Systems Command, United States Air Force.

BOGDANOFF, D.W. 1983 Compressibility effects in turbulent shear layers. *AIAA J.* **21** (6), 926–927.

CARPENTER, P.W. & GREEN, P.N. 1997 The aeroacoustics and aerodynamics of high-speed Coanda devices, part 1: conventional arrangement of exit nozzle and surface. *J. Sound Vib.* **208** (5), 777–801.

CORNELIUS, K.C. & LUCIUS, G.A. 2012 Physics of Coanda jet detachment at high-pressure ratio. *J. Aircraft* **31** (3), 591–596.

CROWTHER, W.J., WILDE, P.I.A., GILL, K. & MICHIE, S.M. 2009 Towards integrated design of fluidic flight controls for a flapless aircraft. *Aeronaut. J.* **113** (1149), 699–713.

CUNFF, C.L. & ZEBIB, A. 1996 Nonlinear spatially developing Görtler vortices in curved wall jet flow. *Phys. Fluids* **8** (9), 2375–2384.

DEANE, A.E., KEVREKIDIS, I.G., KARNIADAKIS, G.E. & ORSZAG, S.A. 1991 Low-dimensional models for complex geometry flows: application to grooved channels and circular cylinders. *Phys. Fluids* A **3** (10), 2337–2354.

DUNAEVICH, L. & GREENBLATT, D. 2020 Stability and transition on a Coanda cylinder. *Phys. Fluids* **32** (8), 084106.

ENGLAR, R.J., HEMMERLY, R.A., TAYLOR, D.W., MOORE, W.H., SEREDINSKY, V., VALCKENAERE, W. & JACKSON, J.A. 1981 Design of the circulation control wing STOL demonstrator aircraft. *J. Aircraft* **18** (1), 51–58.

FAN, C.C., XIAO, X., EDWARDS, J.R., HASSAN, H.A. & BAURLE, R.A. 2004 Hybrid large-eddy/Reynolds-averaged Navier–Stokes simulation of shock-separated flows. *J. Spacecr. Rockets* **41** (6), 897–906.

FERLAUTO, M. & MARSILIO, R. 2017 Numerical investigation of the dynamic characteristics of a dual-throat-nozzle for fluidic thrust-vectoring. *AIAA J.* **55** (1), 86–98.

FORSTER, M., BIAVA, M. & STEIJL, R. 2016 Multipoint optimisation of Coanda surfaces for transonic circulation control using the adjoint method. In *8th AIAA Flow Control Conference*, p. 3773.

FORSTER, M. & STEIJL, R. 2017 Design study of Coanda devices for transonic circulation control. *Aeronaut. J.* **121** (1243), 1368–1391.

FUJISAWA, N. & KOBAYASHI, R. 1987 Turbulence characteristics of wall jets along strong convex surfaces. *Intl J. Mech. Sci.* **29** (5), 311–320.

GREGORY-SMITH, D.G. & GILCHRIST, A.R. 1987 The compressible Coanda wall jet—an experimental study of jet structure and breakaway. *Intl J. Heat Fluid Flow* **8** (2), 156–164.

GREGORY-SMITH, D.G. & SENIOR, P. 1994 The effects of base steps and axisymmetry on supersonic jets over Coanda surfaces. *Intl J. Heat Fluid Flow* **15** (4), 291–298.

GÖRTLER, H. 1941 Instabilitat laminarer grenzchichten an konkaven wanden gengenuber gewissen deeidimensionalen storungen. *Z. Angew. Math. Mech.* **21** (4), 250–252.

HAN, G., DE ZHOU, M. & WYGNANSKI, I. 2006 On streamwise vortices and their role in the development of a curved wall jet. *Phys. Fluids* **18** (9), 1.

HARLEY, C., WILDE, P. & CROWTHER, W. 2009 Application of circulation control manoeuvre effectors for three axis control of a tailless flight vehicle. In *47th AIAA Aerospace Sciences Meeting including The New Horizons Forum and Aerospace Exposition*, p. 146.

HOHOLIS, G., STEIJL, R. & BADCOCK, K. 2016 Circulation control as a roll effector for unmanned combat aerial vehicles. *J. Aircraft* **53** (6), 1875–1889.

HUTCHIN, C. 2019 NATO AVT-239 task group: control effectiveness and system sizing requirements for integration of fluidic flight controls on the SACCON aircraft configuration. *AIAA Scitech 2019 Forum*.

JIANG, Y., ZHANG, L., HUANG, Y., GAO, L. & CHEN, H. 2018 Lift response characteristics of a circulation control airfoil with internally blown flap. *Acta Aeronaut. Astronaut. Sin.* **39** (7), 121807.

KONISHI, Y. & ASAI, M. 2010 Development of subharmonic disturbance in spanwise-periodic low-speed streaks. *Fluid Dyn. Res.* **42** (3), 035504.

LI, L., HIROTA, M., OUCHI, K. & SAITO, T. 2017 Evaluation of fluidic thrust vectoring nozzle via thrust pitching angle and thrust pitching moment. *Shock Waves* **27** (1), 53–61.

LIKHACHEV, O., NEUENDORF, R. & WYGNANSKI, I. 2001 On streamwise vortices in a turbulent wall jet that flows over a convex surface. *Phys. Fluids* **13** (6), 1822–1825.

LIU, X.D., OSHER, S. & CHAN, T. 1994 Weighted essentially non-oscillatory schemes. *J. Comput. Phys.* **115** (1), 200–212.

LLOPIS-PASCUAL, A. 2017 Supercritical Coanda jets for flight control effectors. PhD thesis, Manchester University, Manchester.

LUMLEY, J.L. 1967 The structure of inhomogeneous turbulent flows. In *Atmospheric Turbulence and Radio Wave Propagation*, pp. 166–178. Nauka.

MATSSON, O. & JOHN, E. 1998 Görtler vortices in wall jet flow on a rotating cylinder. *Phys. Fluids* **10** (9), 2238–2248.

MENTER, F.R. 1994 Two-equation eddy-viscosity turbulence models for engineering applications. *AIAA J.* **32**, 1598–1605.

MOIN, P. & MAHESH, K. 1998 Direct numerical simulation: a tool in turbulence research. *Annu. Rev. Fluid Mech.* **30** (1), 539–578.

NAQAVI, I.Z., TYACKE, J.C. & TUCKER, P.G. 2018 Direct numerical simulation of a wall jet: flow physics. *J. Fluid Mech.* **852**, 507–542.

NEUENDORF, R., LOURENCO, L. & WYGNANSKI, I. 2004 On large streamwise structures in a wall jet flowing over a circular cylinder. *Phys. Fluids* **16** (7), 2158–2169.

NEUENDORF, R. & WYGNANSKI, I. 1999 On a turbulent wall jet flowing over a circular cylinder. *J. Fluid Mech.* **381**, 1–25.

PANDEY, A. & GREGORY, J.W. 2020 Instabilities and turbulence in a forced turbulent convex wall jet. *Phys. Fluids* **32** (9), 095111.

PANDEY, A. & GREGORY, J.W. 2021 Spanwise wavelength of streamwise vortices in a forced turbulent convex wall jet. *AIAA J.* **58** (1), 1–6.

PAPAMOSCHOU, D. & ROSHKO, A. 1988 The compressible turbulent shear layer: an experimental study. *J. Fluid Mech.* **197**, 453–477.

QU, F., CHEN, J., SUN, D., BAI, J. & ZUO, G. 2019*a* A grid strategy for predicting the space plane's hypersonic aerodynamic heating loads. *Aerosp. Sci. Technol.* **86**, 659–670.

QU, F. & SUN, D. 2017 Investigation into the influences of the low-speed flows' accuracy on RANS simulations. *Aerosp. Sci. Technol.* **70**, 578–589.

QU, F., SUN, D., HAN, K., BAI, J., ZUO, G. & YAN, C. 2019*b* Numerical investigation of the supersonic stabilizing parachute's heating loads. *Aerosp. Sci. Technol.* **87**, 89–97.

SANDHAM, N.D. 1991 Three-dimensional simulations of large-eddies in compressible mixing layer. *J. Fluid Mech.* **224** (2), 177.

SCHLATTER, P., BRANDT, L., DE LANGE, H.C. & HENNINGSON, D.S. 2008 On streak breakdown in bypass transition. *Phys. Fluids* **20** (10), 101505.

SMITH, D.R. & WARSOP, C. 2019 NATO AVT-239 task group: 'innovative control effectors for manoeuvring of air vehicles'–introduction and overview. *AIAA Scitech 2019 Forum*.

SPALART, P.R., DECK, S., SHUR, M.L., SQUIRES, K.D., STRELETS, M.K. & TRAVIN, A. 2006 A new version of detached-eddy simulation, resistant to ambiguous grid densities. *Theor. Comput. Fluid Dyn.* **30** (3), 20.

SUN, D., QU, F., LIU, C., YAO, F. & BAI, J. 2020 Numerical study of the suction flow control of the supersonic boundary layer transition in a framework of gas-kinetic scheme. *Aerosp. Sci. Technol.* **109** (2), 106397.

SUN, D., QU, F. & YAN, C. 2018 An effective flux scheme for hypersonic heating prediction of re-entry vehicles. *Comput. Fluids* **176**, 109–116.

SUN, M., SANDHAM, N.D. & HU, Z. 2019 Turbulence structures and statistics of a supersonic turbulent boundary layer subjected to concave surface curvature. *J. Fluid Mech.* **865**, 60–99.

WANG, P.C. & MCGUIRK, J.J. 2013 Large Eddy Simulation of supersonic jet plumes from rectangular con-di nozzles. *Intl J. Heat Fluid Flow* **43**, 62–73.

WANG, Q., QU, F., SUN, D. & BAI, J. 2023 Numerical study of instabilities and compressibility effects on supersonic jet over a convex wall. *J. Fluid Mech.* **954**, A6.

WANG, Q., QU, F., ZHAO, Q. & BAI, J. 2022 Numerical study of the hysteresis effect on the supercritical airfoil for the transonic circulation control. *Aerosp. Sci. Technol.* **126**, 107645.

WANG, Q.C., WANG, Z.G., SUN, M.B., YANG, R., ZHAO, Y.X. & HU, Z. 2019 The amplification of large-scale motion in a supersonic concave turbulent boundary layer and its impact on the mean and statistical properties. *J. Fluid Mech.* **863**, 454–493.

WARSOP, C., CROWTHER, W. & FORSTER, M. 2019 NATO AVT-239 task group: supercritical Coanda based circulation control and fluidic thrust vectoring. *AIAA Scitech 2019 Forum*.

WARSOP, C. & CROWTHER, W.J. 2018 Fluidic flow control effectors for flight control. *AIAA J.* **56** (10), 1–17.

WATANABE, T. & NAGATA, K. 2021 Large-scale characteristics of a stably stratified turbulent shear layer. *J. Fluid Mech.* **927**.

WILDE, P., BUONANNO, A., CROWTHER, W. & SAVVARIS, A. 2008 Aircraft control using fluidic maneuver effectors. In *26th AIAA Applied Aerodynamics Conference*.

WILLIAMS, D.R., SEIDEL, J., OSTEROOS, R. & MCLAUGHLIN, T.E. 2019 NATO AVT-239 task group: flight control derivatives using active flow control effectors on the ICE/SACCON UAS model. *AIAA Scitech 2019 Forum*.

YOON, S. & JAMESON, A. 1988 Lower-upper Symmetric-Gauss-Seidel method for the Euler and Navier–Stokes equations. *AIAA J.* **26** (9), 1025–1026.

ZHANG, D., TAN, J. & LI, H. 2017 Structural characteristics of supersonic mixing enhanced by introducing streamwise vortices. *Appl. Phys. Lett.* **111** (11), 114103.